Geophys. J. Int. (–) –, 1–??

Relating teleseismic backprojection images to earthquake kinematics

Jiuxun Yin[1], Marine A. Denolle[1]
[1] *Department of Earth and Planetary Sciences, Harvard University, Cambridge, MA, USA*

Received –; in original form –

0 SUMMARY

Backprojection (BP) of teleseismic P waves is a powerful tool to study the evolution of seismic radiation of large earthquakes. The common interpretations on the BP results are qualitative comparisons with earthquake kinematic observations, such as the evolution of slip on the fault and rupture velocity. However, the direct relation between the BP images and physical properties of the earthquake rupture process remains unclear and is needed for further application of this technique. In this study, we start from a theoretical formulation of the BP images, which is linear in the frequency domain, and carry on a synthetic exercise with kinematic source representations and virtual receivers embedded in a homogeneous fullspace. We find that the fundamental linear formulation of the BP method is most correlated with the true kinematic source properties: in frequency domain the BP images are proportional to the images of slip motion through a scaling matrix $\mathbf{F}(\omega)$ that accounts for radiation pattern and source-receiver geometry and that acts as a spatial smoothing operator. Overall, the synthetic BP images match relatively well the kinematic models and our exercise validates that the BP image can be directly used to track the spatio-temporal propagation of rupture front. However, because $\mathbf{F}(\omega)$ is not strictly an identity matrix due to limited station coverage in space (azimuth and distance) and to the limited frequency bands of the seismograms, it remains difficult to recover the details in the rupture fronts from BP images. We define a resolvability parameter $\epsilon_I(\omega)$ built from $\mathbf{F}(\omega)$ that incorporates fault geometry, radiation pattern, and wave propagation (source-array geometry) to quantify the ability of the BP method to resolve details of the rupture on the fault. $\epsilon_I(\omega)$ successfully captures the similarity between BP images and kinematic source. We analyze the resolvability of most tectonically active regions and the most commonly used seismic arrays. Based on this global resolvability analysis, we propose an empirical relation between the seismic frequency, resolvable area, and earthquake magnitude. It provides general guidelines to choose the lowest frequency in seismic waveform (for example, about 0.3 Hz for M_w 8 and 1 Hz for M_w 7 earthquakes) and to interpret the BP image in terms of the source kinematics. In general, this work attempts to provide a clear interpretation of the BP images in light of the real earthquake rupture process and give a systematic evaluation of seismic data limitations.

keywords: backprojection, rupture process, pseudo-dynamic source, seismic arrays

1 INTRODUCTION

With the development of dense seismic arrays (e.g., Hi-net in Japan (Okada et al. 2004; Obara et al. 2005); USArray (Earthscope program)), seismologists are able to harness key information of earthquake sources from seismic waveform coherency. The backprojection (BP) of high-frequency teleseismic P waves (usually from 0.1 to 4 Hz) is a method widely used to study the evolution of earthquake rupture and has been particularly effective for the study of large earthquakes. It provides relative location of the seismic radiation coherency on the projection of the fault plane at the hypocentral depth. Its application to the recent large earthquakes ($M_w > 8$) has succeeded in characterizing a spatio-temporal evolution of seismic radiation of earthquakes (e.g., Ishii et al. 2005, 2007; Xu et al. 2009; Kiser et al. 2011; Meng et al. 2011; Yao et al. 2011; Yagi et al. 2012; Yao et al. 2012; Fan & Shearer 2015; Wang et al. 2016; Yin et al. 2017, 2018). BP in general requires fewer assumptions than kinematic slip inversions that necessitates, for example, fault geometry, slip-rate function shapes (Ji et al. 2002a,b), and rupture velocity in some cases (Kikuchi & Kanamori 1982). In addition, the simplicity of the method allows for rapid calculations. Therefore, preliminary information about earthquake rupture processes can be rapidly obtained from waveform data, soon after the seismic waves arrive at the array of receivers (e.g., Incorporated Research Institutions for Seismology Data Management Center (IRIS DMC), 2011). Despite the success of the BP approach, the physical interpretation of the images in terms of rupture properties is yet to be verified.

While the BP images are the spatial and temporal distributions of high frequency waveform coherency, they are often referred to as relative radiated energy (Ishii et al. 2007) and/or energy burst (Yao et al. 2012). Qualitative comparisons between BP results and independent kinematic inversions for the recent large earthquake events exhibit some spatial and temporal correlation between the BP images and the source kinematic evolution (e.g., Koper et al. 2011; Wang & Mori 2011; Lay et al. 2012; Uchide et al. 2013; Yagi & Okuwaki 2015; Avouac et al. 2015; Melgar et al. 2016; Yin et al. 2016, 2017). In particular, the BP results constructed from low frequency waves (about 0.1-0.5 Hz) are mostly collocated with large coseismic slip and thus to negative coseismic shear stress change (stress drop) (Melgar et al. 2016; Yin et al. 2016, 2017). In contrast, the BP results constructed from the high frequency seismic waves (0.5-1 Hz) are consistent with the edges of large slip areas, and thus with the positive stress change (stress loading).

The temporal evolution of the earthquake seismic radiated energy, or seismic power, may be related to specific locations on the fault with the help of BP images: Denolle et al. (2015) and Yin et al. (2018) apply a time-varying spectral analysis to calculate the time history of earthquake radiated energy and directly compare it with BP results, showing the correlation between high coherency and high radiated energy. However, these comparisons remain qualitative, and the interpretation of BP images with respect to seismic energy or excitation is yet to be investigated.

A first element to discuss is the physical dimensions of the BP image. The BP algorithm involves the alignment and stacking of observed seismic waveforms. Therefore, the BP approach is essentially a manipulation of the seismic data, and the BP images carry the physical units of the data. Fukahata et al. (2014) present a theoretical framework on the relationship between the BP results and a classical linear inversion solution. They focus on the conventional BP (Ishii et al. 2005, 2007) and Hybrid BP (Yagi et al. 2012) methods with linear stacking. They suggest that these BP images represent the slip motion on a fault, thereby approximately equal to a kinematic slip inversion, provided that the Green's function is sufficiently close to a shifted delta function. These conclusions are enlightening to understand the dimension of the BP images. However, their deductions rely on the assumption of strong decorrelation between source locations other than the true source. That is, whether the correlation between Green's functions from multiple sources to a single receiver is delta function in space. This assumption on decorrelation may not hold as it is widely used in seismic interferometry analysis (Campillo & Paul 2003).

A second element to discuss is the ability of BP methods to resolve small wavelengths features in source radiation in various frequency bands. One of the conventional approaches to quantify resolution is to perform the seismic array response (Rost & Thomas 2002). The array response carries important information about the limitations in spatial resolution of a seismic array toward specific region; it represents the BP image given a delta source in time and space. Another method to test the resolution of a BP method is to setup a series of synthetic point sources with different locations and/or source times, then to apply the BP method and see whether these point sources can be correctly recovered (e.g., Yao et al. 2011; Meng et al. 2011; Wang et al. 2016; Yin & Yao 2016; Yin et al. 2018). These synthetic tests are popular to establish the spatial resolution limits of BP. Another example of such exercise is how Wang et al. (2016) integrate these two approaches. They express the BP images as the convolution of an array response and a series of point sources, and then attempt to solve for the high-frequency radiators (source series) through an inversion scheme. However, and in general, an instantaneous point-source representation of the on-fault radiation may not be appropriate and the process zone (zone of active slip) is likely distributed in realistic earthquakes.

Addressing these two elements is necessary to interpret source physics from the BP images and to better apply the BP methodology to study earthquake ruptures. Specifically, the physical unit of the BP image determines whether we can interpret the BP images as snapshot of slip motions; the BP resolution controls whether, and how well, we can use the BP images to map rupture propagation (i.e. for appropriate estimate of rupture velocity).

Realistic kinematic source generators provide great opportunities to investigate the relation between BP images and kinematic properties. This study attempts to address the elements mentioned above using synthetic waveforms. We restrict our discussion to idealistic wave propagation in a homogeneous full space in order to focus on the relation between source and seismic waveforms and ignore the effects of 3D elastic structure (and Green's function) that might alter the results (see, for instance, Ishii et al. 2007; Meng et al. 2016; Yue et al. 2017). In a homogeneous full space there are (i) analytical formulations of the far-field body waves (Aki & Richards 2002) and (ii) reliable kinematic source representations (in this study, we use the kinematic source generator developed by Liu et al. 2006; Schmedes et al. 2013; Crempien & Archuleta 2014). Moreover, we consider the simplest approach to backprojection, that is, the linear stacking in the Fourier domain. This framework enables a direct reading of the BP image in light of the source slip-rate functions. Given this linear formulation, we propose a simple scalar metric to quantify the BP resolution solely based on the source-receiver geometry and for a given seismic frequency. Then, we test the linear BP images against realistic and heterogeneous kinematic sources. Finally, we extend these theoretical formulations to explore realistic limitations of BP techniques given the distribution of global seismicity and of globally available seismic arrays.

2 METHODS

2.1 Synthetic seismograms for kinematic sources

In the homogeneous full space, the direct teleseismic P-wave displacement seismograms $d_k(t)$ recorded by the k^{th} station can be regarded as the summation over the fault plane (or source) of individual slip-rate functions $\dot{u}_n(t)$ (subfault n) with terms of radiation pattern R^P_{kn}, geometrical spreading, and travel-time delay t_{kn} (Aki & Richards 2002):

$$d_k(t) = \sum_{n=1}^{N} \frac{R^P_{kn}}{4\pi\rho\alpha^3} \frac{\mu\Delta S}{r_{kn}} \dot{u}_n(t - t_{kn}), \tag{1}$$

where r_{kn} is the distance from the n^{th} subfault to the k^{th} station; ρ, α, and μ are the density, P-wave velocity and shear modulus in the source region, respectively. ΔS is the area of the subfault.

This is a discretized formulation of the representation theorem (Burridge & Knopoff 1964) applied in the far field for a source with known slip history. After a Fourier transform, the travel-time delays become phase shifts $e^{-i\omega t_{kn}}$ at the angular frequency ω,

$$D_k(\omega) = \sum_{n=1}^{N} \frac{R^P_{kn}}{4\pi\rho\alpha^3} \frac{\mu\Delta S}{r_{kn}} e^{-i\omega t_{kn}} \dot{U}_n(\omega). \tag{2}$$

Given the linearity of the formulation in the frequency domain, we form an vectorial representation to incorporate seismograms from an array of stations (seismogram spectra):

$$\begin{bmatrix} D_1(\omega) \\ D_2(\omega) \\ \vdots \\ D_K(\omega) \end{bmatrix} = \mathbf{A}(\omega) \begin{bmatrix} \dot{U}_1(\omega) \\ \dot{U}_2(\omega) \\ \vdots \\ \dot{U}_N(\omega) \end{bmatrix}, \tag{3}$$

where the wave propagation matrix $\mathbf{A}(\omega)$ is:

$$\mathbf{A}(\omega) = \frac{\mu\Delta S}{4\pi\rho\alpha^3} \times \begin{bmatrix} \frac{R^P_{11}}{r_{11}} e^{-i\omega t_{11}} & \cdots & \frac{R^P_{1N}}{r_{1N}} e^{-i\omega t_{1N}} \\ \frac{R^P_{21}}{r_{21}} e^{-i\omega t_{21}} & \cdots & \frac{R^P_{2N}}{r_{2N}} e^{-i\omega t_{2N}} \\ \vdots & \ddots & \vdots \\ \frac{R^P_{K1}}{r_{K1}} e^{-i\omega t_{K1}} & \cdots & \frac{R^P_{KN}}{r_{KN}} e^{-i\omega t_{KN}} \end{bmatrix}_{K\times N}. \tag{4}$$

Being a linear operator in the frequency domain, the vectorial formulation of Eq.(4) is convenient to separate the two main variables that constitute a seismogram: the source term with the slip-rate function $\dot{U}_n(\omega)$ and the wave-propagation term $\mathbf{A}(\omega)$. The latter can be revised to accommodate radiation pattern, geometrical spreading, and travel-time elements calculated in a

3D Earth model. The linear BP in the frequency domain is similar to beamforming (e.g., Rost & Thomas 2002; Wang et al. 2016; Yin & Yao 2016). In the practical application of frequency-domain BP, the waveform data are windowed and Fourier transformed to construct Eq.(3). This provides the temporal dependence of the BP images.

2.2 Formulation of linear BP in the frequency domain

The two key ingredients of BP are waveform alignment and stacking (Ishii et al. 2005). The literature is rich in method development to improve both ingredients (e.g., Walker et al. 2005; Ishii et al. 2007; Xu et al. 2009; Meng et al. 2012a; Yagi et al. 2012; Yao et al. 2012; Zhang et al. 2016; Meng et al. 2016). The alignment in our synthetic exercise is known and trivial. The linear stacking scheme is chosen in order to relate source kinematics to BP images, which differs from other studies that may favor nonlinear n^{th}-root stacking scheme to enhance resolution.

The alignment and linear stacking are carried out by multiplying a phase-shift matrix $\tilde{\mathbf{A}}(\omega)$ to the left hand side of $\mathbf{D}(\omega)$ in Eq.(3):

$$\tilde{\mathbf{A}}(\omega) = \begin{bmatrix} e^{i\omega t_{11}} & e^{i\omega t_{21}} & \dots & e^{i\omega t_{K1}} \\ e^{i\omega t_{12}} & e^{i\omega t_{22}} & \dots & e^{i\omega t_{K2}} \\ \vdots & \ddots & \ddots & \vdots \\ e^{i\omega t_{1N}} & e^{i\omega t_{2N}} & \dots & e^{i\omega t_{KN}} \end{bmatrix}_{N\times K} \mathbf{W}, \tag{5}$$

where the matrix $\mathbf{W}$ is a $K \times K$ diagonal matrix that is used in linear weighted stack to balance the contributions of seismograms. The weighting matrix $\mathbf{W}$ is usually applied to normalize the different amplitude of waveforms or adjust the uneven distribution of stations in a seismic array (e.g. Walker et al. 2005; Walker & Shearer 2009; Yao et al. 2012). In this example, we apply uniform averaging by choosing $\mathbf{W} = \frac{1}{K}\mathbf{I}$ for the evenly distributed synthetic array and omit it in the following discussion. In practice, the travel-time terms in the $\tilde{\mathbf{A}}(\omega)$ are theoretically calculated based on a specific Earth velocity model. Therefore, we can obtain the BP results, or we call BP image at frequency ω:

$$\mathbf{U}^{BP}(\omega) = \tilde{\mathbf{A}}(\omega)\mathbf{D}(\omega) = \tilde{\mathbf{A}}(\omega)\mathbf{A}(\omega)\dot{\mathbf{U}}(\omega) = \mathbf{F}(\omega)\dot{\mathbf{U}}(\omega). \tag{6}$$

This simple form provides a linear relation in the frequency domain between the BP image constructed from displacement seismograms $\mathbf{U}^{BP}(\omega)$ and slip-rate field on the fault surface $\dot{\mathbf{U}}(\omega)$. Specifically, the BP image should be proportional to the band-pass filtered slip-rate field. The scaling factor is the matrix $\mathbf{F}(\omega) = \tilde{\mathbf{A}}(\omega)\mathbf{A}(\omega)$, which is a frequency dependent function of the source-array geometry, wave propagation effects, and radiation pattern (Fig.1 (a)-(c)). Note that $\tilde{\mathbf{A}}(\omega)$ is not $\mathbf{A}(\omega)^{-1}$, which would turn the problem into a kinematic slip inversion. Instead, $\mathbf{F}(\omega)$ bears great similarity with the array response: each column is the array response to an impulse source at a particular source location with specific radiation pattern terms (Fig.1 (d)-(f)). We refer to $\mathbf{F}(\omega)$ as the resolution matrix because of its spatial smoothing effects on the slip-rate field at a specific frequency ω. The closer $\mathbf{F}(\omega)$ is to identity, the greater the similarity between BP image and slip-rate field. We thus proceed to investigate the impact of $\mathbf{F}(\omega)$ onto interpreting the slip-rate distribution from BP images. Fig.1 (a)-(c) shows an example of

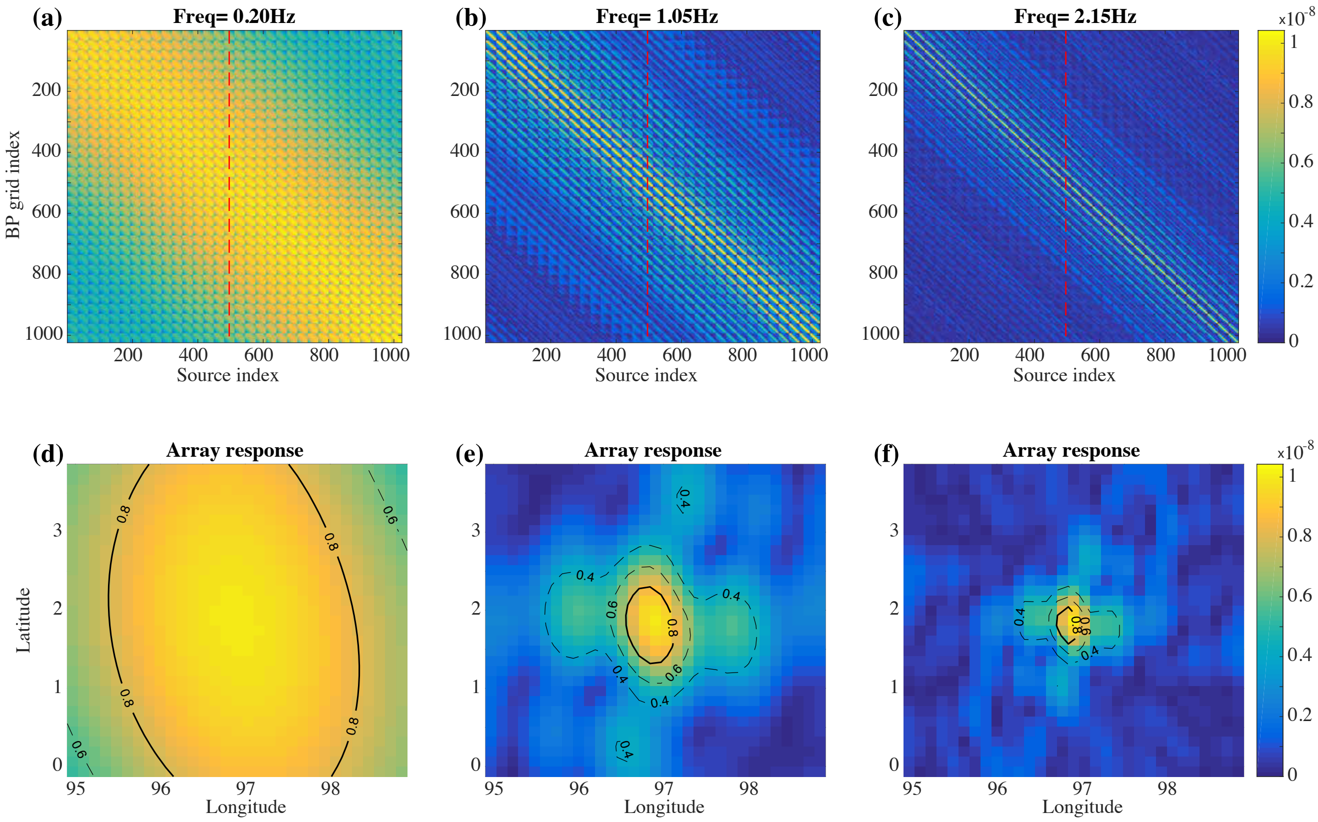

Figure 1. Absolute value of the resolution matrices of the Hi-Net array toward IDN2 region (see location in Figure 7) at (a) 0.2 Hz; (b) 1.05 Hz and (c) 2.15 Hz. (d)-(e) show the corresponding array response at the source location indicated by the red dashed lines in the top panels. Contours indicate the 0.4, 0.6 and 0.8 of the maximum value.

$\mathbf{F}(\omega)$: it varies in shape as it converges to diagonal with increasing seismic frequency. To quantify the similarity between the resolution and identity matrices, we define the resolvability parameter ϵ_I as the 2D correlation coefficient between the $\mathbf{F}(\omega)$ and an identity matrix with same size:

$$\epsilon_I(\omega) = |corr2(\mathbf{F}, \mathbf{I})| = \frac{|\sum_m \sum_n (F_{mn} - \bar{F})(I_{mn} - \bar{I})|}{\sqrt{[\sum_m \sum_n (F_{mn} - \bar{F})^2][\sum_m \sum_n (I_{mn} - \bar{I})^2]}}, \tag{7}$$

m, n being the elements of the matrices. $\epsilon_I(\omega)$ varies between 0 and 1 and provides a compact form to quantify the resolution of linear BP for specific array settings and the deterioration effects of the source-receiver geometry on the BP image. We refer to $\epsilon_I(\omega)$ as measure of resolvability. It does not carry the units of spatial resolution, instead it encapsulates multiple parameters relevant to BP processing. This choice bears some similarity with other metrics, such as the Goodness-Of-Fit criteria that combines multiple ground motion metrics to quantify broadband waveform fitting (Olsen & Mayhew 2010).

3 BACKPROJECTION ON KINEMATIC SOURCES

We test the linear BP method using the theoretical formulation of Eq.(6) and its usefulness in interpreting kinematic properties on synthetic sources that has kinematic complexity.

3.1 Synthetic example set up

A pseudo-dynamic source model is a statistical representation of the source built upon the correlations among kinematic parameters found in earthquake dynamic models (Mai & Beroza 2002; Schmedes et al. 2010). We use a kinematic source generator developed by Liu et al. (2006) and Crempien & Archuleta (2014). The kinematic source parameters are local slip, rise time, rupture velocity, peak time. After a spatial discretization of the fault plane, we obtain a series of correlated distributions of seismic moment, rupture velocity, and rise time (Supplement Fig.S1). Onset time, which is the time when each subfault begins to slip, is calculated using the wave equation on the rupture velocity field (Frankel 2009). We use the moment-rate function defined in Liu et al. (2006):

$$\dot{u}(t) = \begin{cases} C_N[0.7 - 0.7\cos(\pi t/\tau_1) + 0.6\sin(0.5\pi t/\tau_1)] \qquad (0 \leq t < \tau_1) \\ C_N[1.0 - 0.7\cos(\pi t/\tau_1) + 0.3\cos(\pi(t-\tau_1)/\tau_2)] \qquad (\tau_1 \leq t < 2\tau_1), \\ C_N[0.3 + 0.3\cos(\pi(t-\tau_1)/\tau_2)] \qquad (2\tau_1 \leq t < \tau) \end{cases} \tag{8}$$

where $C_N = \pi/(1.4\pi\tau_1 + 1.2\tau_1 + 0.3\pi\tau_2)$ is a normalization constant, τ is the rise time, $\tau_1 = 0.3\tau$ is the peak time and $\tau_2 = \tau - \tau_1 = 0.7\tau$. Therefore, the n^{th} subfault patch on the fault surface has the corresponding slip-rate function:

$$\dot{u}_n(t) = \dot{u}(t - t_0^n)M_0^n/(\mu\Delta S), \tag{9}$$

where t_0^n and M_0^n are the onset time and seismic moment at the n^{th} subfault, respectively. The total seismic moment of these pseudo-dynamic sources corresponds to M_w 8, above which magnitude the BP methods is generally applied and seem to work best (more details are discussed in the section 4 and section 5.4).

The synthetic seismograms are constructed from the slip history of each source model. To focus on source rather than wave propagation effects, we keep wave propagation simple and embed the source in a homogeneous full space (Fig.2 (a)) of elastic properties density $\rho = 2,700$ kg/m^3; shear modulus $\mu = 2.43$ GPa; P and S wave velocity are $V_P = 5.2$ km/s and $V_S = 3.0$ km/s, respectively. Eq.(1) then allows us to numerically compute the direct P-wave seismic waveforms for a specific array of receivers. The focal mechanism at each subfault is a pure shear double couple with $15°$ dip angle, $0°$ strike angle, and $90°$ rake angle to render the typical slip direction of megathrust earthquakes. We strategize to place the synthetic receivers beneath the synthetic source to mimic the steep takeoff angles of teleseismic P waves ($15° - 30°$, see Fig.2 (a) and Fig.3 (a)). Rupture velocity information can be inferred from directivity effects. Therefore, we apply the linear BP method for the synthetic source with two types of seismic arrays: (i) arrays Toward1 and Toward2, both located ahead of the rupture direction; (ii) arrays Away1 and Away2, both located behind the direction of rupture. In each type of arrays, we also design

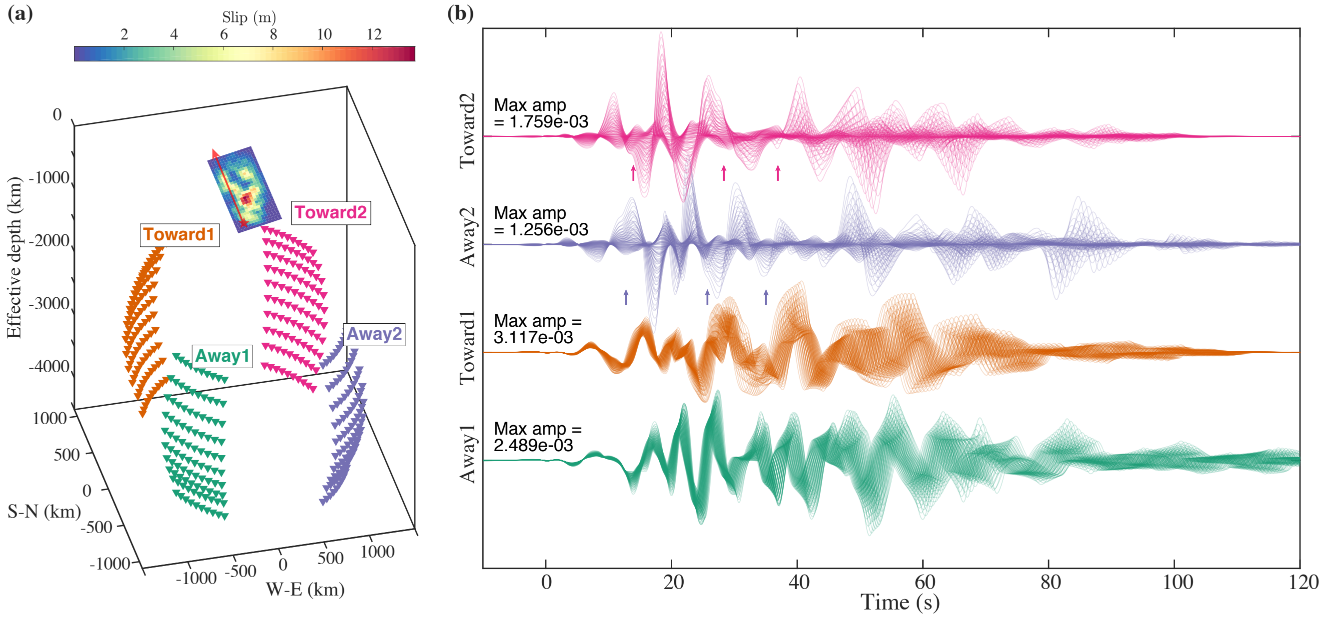

Figure 2. Synthetic example: (a) Final slip distribution of a kinematic source model (colorscale) as well as locations of the 4 seismic arrays (colored triangles) embedded in the homogeneous full space. The spatial dimensions of the source are exaggerated 5 times for better view. The red star and arrow indicate the location of the hypocenter and the overall direction of rupture propagation, respectively. (b) Synthetic waveforms filtered [0.1 1] Hz recorded by each array. The numbers indicate the maximum waveform amplitudes in each array. Arrows indicates some unsystematic polarity shifting of array waveforms due to rupture propagation (Also see Supplement Fig.S2).

the locations of two arrays to sample different parts of the radiation patterns: Set1 with those labeled 1 (Toward1 and Away1) have rays that sample the same quadrant of the P-wave radiation pattern (i.e. identical polarity) while the Set2 arrays labeled 2 (Toward2 and Away2) mostly sample the P-wave nodal plane (Fig.3 (a)). We adjust the distance to the kinematic source with the known takeoff and azimuth angles of each virtual station (Fig.3 (a)) and make the travel time identical to those calculated from the IASP91 1D Earth velocity model (Fig.3 (b), the velocity model is from Kennett & Engdahl (1991)). All these settings aim to keep the synthetic BP tests resembling the real applications. It is intuitive that Set2, which samples the nodal plane, is greatly impaired by waveform de-coherence (Fig.2 (b)) among virtual receivers and thus produce a low resolvability $\epsilon_I(\omega)$.

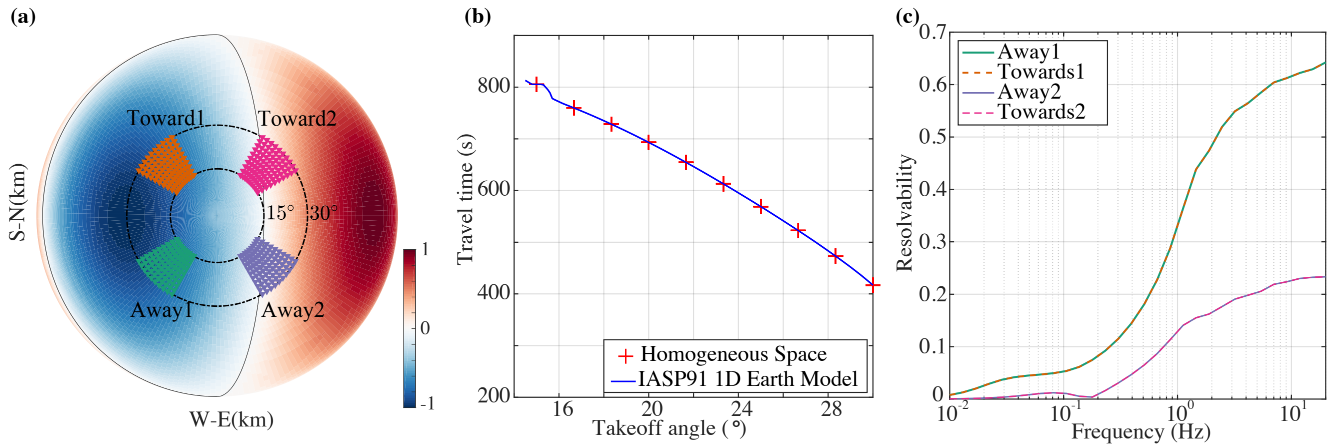

Figure 3. Takeoff angle distributions and BP resolvability of the four synthetic arrays: (a) Focal mechanism (lower hemisphere) of the synthetic source as well as the projection of takeoff ray path of each stations in bird's-eye view. The focal mechanism is color-coded by the radiation pattern and the nodal planes are also indicated by the black thin lines. The two dashed circles show the 10° and 30° takeoff angles, respectively. (b) Blue curve shows the P-wave takeoff angle against travel time based on the IASP91 1D Earth velocity model (Kennett & Engdahl 1991). Red crosses indicate the same setup for the synthetic arrays in the homogeneous full space (Fig.2 (a)). (c) BP resolvability $\epsilon_I(\omega)$ calculated for each array. Array colors are the same as in Fig.2

We apply the basic linear BP method described in Section 2.2 to these synthetic waveforms, which we filter in several narrow frequency bands within 0.1 to 1 Hz. We slide through the waveforms with a 20% Tukey window taper (20% total window length for the cosine taper) every time step of 0.5 s. The length of time window is chosen as 4 times of longest period ($4/f_{min}$ seconds) of the bandpass filters (40 s: 0.1-0.2 Hz; 20 s: 0.2-0.4 Hz; 10 s: 0.4-0.7 Hz; 6 s: 0.7-1 Hz) to capture enough periods in the waveforms. Then, we transform the windowed waveforms to frequency domain, obtain the synthetic data spectra $\mathbf{D}(\omega)$, and calculate the corresponding phase-shift matrix $\tilde{\mathbf{A}}(\omega)$ for the pre-defined source location. Therefore, we can obtain the BP images at each frequency ω and for each time window (Eq.(6)). It is common in frequency-domain backprojection to correct the window time to the appropriate source time: the motion of a source stretches of the seismic signal that distorts the windowing time axis (similar to Doppler effects, see the directivity effects in waveforms in Fig.2 (b)) and thus requires a time calibration. We apply the same calibration method as introduced by Yin & Yao (2016) (see their Eq.(11)) and use the location of highest BP amplitude to calibrate the window time for the correct source time.

In this controlled experiment, we can directly compare the BP results with the ground truth parametrization of the rupture. Since the relation between BP results and source kinematics is built in the frequency domain (Eq.(6)), it is necessary to combine the BP images at various frequencies and compare with the slip motions in a continuous frequency band. However, we cannot equate the time series of broad-band BP results (i.e. inverse Fourier transform of the BP value at each subfault $\int \mathbf{U}^{BP}(\omega)e^{i\omega t}d\omega$) and slip-rate field (i.e. inverse Fourier transform of $\dot{\mathbf{U}}(\omega)$) simply from Eq.(6) because the resolution matrix $\mathbf{F}(\omega)$ is frequency dependent and is not identity (Fig.1). Instead, we focus on the spatial similarities between the BP images and slip motions distribution of the kinematic sources. We compare the averaged the BP results with all central frequencies (13 discrete frequency values in total: 0.125 Hz, 0.15 Hz, 0.175 Hz, 0.20 Hz, 0.25 Hz, 0.30 Hz, 0.35 Hz, 0.40 Hz, 0.50 Hz, 0.60 Hz, 0.70 Hz, 0.83 Hz, 1.00 Hz) and the filtered slip-rate field within the broader frequency band of 0.1 to 1 Hz. We normalize the BP images at each frequency due to the large differences in the absolute amplitude of these BP results. The frequency-dependent normalization factor is taken as the peak amplitude of the image over the entire source duration. By averaging the normalized BP results over all frequencies, we can obtain the average BP image in the corresponding frequency band. To quantify the similarity between the images, we measure the 2D correlation coefficient (CC) also defined in Eq.(7) between snapshots of the averaged BP image and of the bandpass filtered slip-rate field.

3.2 Results of synthetic backprojection

3.2.1 Resolvability

First, we estimate the resolvability for all four synthetic arrays in the way that was introduced in Section 2.2 Eq.(7) (Fig.2). The resolvability $\epsilon_I(\omega)$ increases with seismic frequency (Fig.3 (c)). Because of the symmetry of the array distributions with respect to the radiation pattern, the resolvability curve of Toward1 and Toward2 overlap with those of Away1 and Away2, respectively.

Moreover, the resolvability of Toward1 and Away1 is systematically higher than Toward2 and Away2 due to better coherency of the waveforms (Fig.2 (b) and Supplement Fig.S2).

Precaution ought to be given to arrays that sample the nodal plane of the focal sphere. The lower resolvability $\epsilon_I(\omega)$ of Set2 indicates the lower BP resolution of seismic arrays near the nodal plane of focal mechanisms due to the source-receiver geometry. Although the early waveform polarity can be manually adjusted by changing the signs of elements in the weighting matrix $\mathbf{W}$, it is difficult to track the later polarity flips due to the propagation of rupture (see arrows in Fig.2 (b) as well as in the Supplement Fig.S2). In addition, moving ruptures induce two effects that might dominate near the nodal planes: i) the moving rupture changes the source-receiver geometry and ii) the radiation pattern is likely to vary due to non-planar fault geometry (for example, the 2002 Denali M_w 7.9 earthquake: Eberhart-Phillips et al. (2003); the 2012 Sumatra M_w 8.6 earthquake: Meng et al. (2012b); and the 2016 Kaikoura M_w 7.8 earthquakes: Duputel & Rivera (2017)). Therefore, delayed polarity flipping can greatly impair waveform coherence and yield poor BP resolution and significant bias in the results. In general, arrays with rays taking off in the vicinity of the nodal planes will be subject to uncertain BP results.

To conclude, the resolvability parameter provides a metric to select array location and confidence in the BP resolution. It incorporates source-receiver geometry and radiation pattern effects present in the resolution matrix $\mathbf{F}(\omega)$ and thus in $\epsilon_I(\omega)$. The resolvability can be easily extended to more complex station distributions like realistic seismic arrays (see later Section 4).

3.2.2 BP images vs slip-rate images

The absolute amplitude of the BP images is controlled by the geometrical spreading and attenuation, which is in general poorly constrained. Resolvability is better at higher frequency, but the displacement and velocity seismograms are dominated by low frequencies due to the long source duration. Thus, we normalize the BP images at each frequency between 0.1 and 1 Hz and average them for each array. Fig.4 shows these images against the known band-passed filtered slip-rate field. Overall, the general features of the BP images are consistent with the evolution of high slip rates (Fig.4). The CC values generally vary between 0.1 to 0.6 (Fig.5 (a) and (b)), which indicates that each array is able to capture relatively well the propagation of rupture on the fault surface, even with lower resolvability. We now discuss the second order disparities among the BP images.

The CCs from Set1 (range 0.2 - 0.6) are systematically higher than those obtained with Set2 (about 0.1 - 0.4), especially during the major stage of moment release in the first 80 s (Fig.5 (a) and (b)). It is expected to occur from the higher resolvability values of Set1. Taking the 10 and 20 s snapshots for example, Set 2 arrays produce 2 peaks instead of the single peak of the slip-rate distribution (Fig.4 (b) and (d)). Therefore, these two peaks are likely artifacts due to the improper source-receiver geometry, i.e. the sampling of the nodal planes on the focal sphere. Because the source directivity effects are expected to occur at equal strength in both Sets, such as those seen in the raw waveforms (Fig.2 (b)), we attribute these first-order differences to the source-receiver geometry, radiation pattern effects, which are captured in ϵ_I (Fig.3 (c)). Therefore, the higher resolvability of Set1 confirms that Set1 is able to better image the slip-rate evolution.

The BP images are also affected by rupture directivity effects. The BP images from the Toward arrays (Fig.4 (a) and (b))

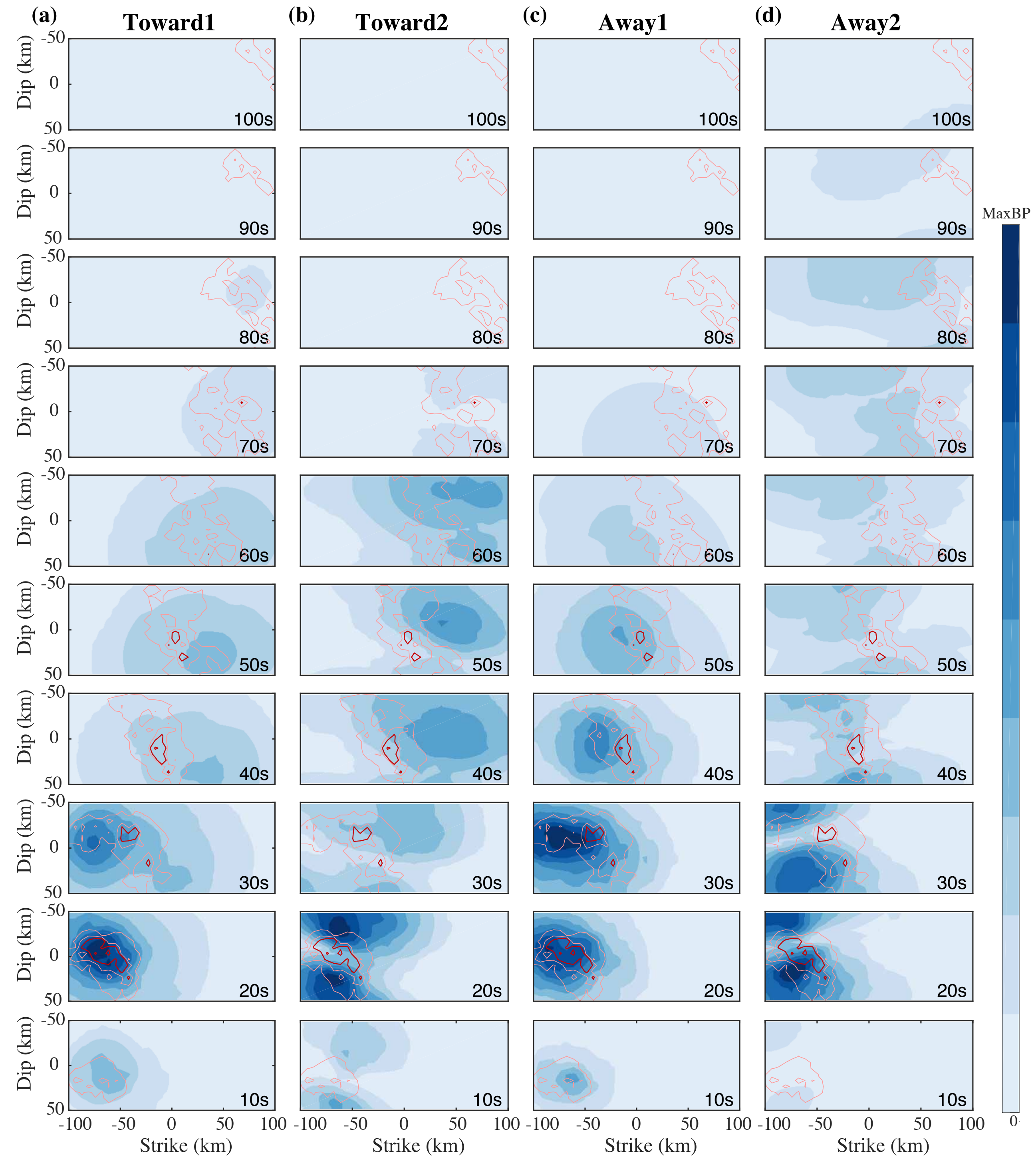

Figure 4. Comparison between the kinematic source model and BP results from (a) Toward1; (b) Toward2 and (c) Away1 and (d) Away2 arrays. The blue colorscale corresponds to the BP image (averaged over frequencies) at each time step. The pink thin contours correspond to 1% and 10% while red bold contours correspond to 20%, 50% and 80% of the maximum amplitude of filtered slip rates.

capture the beginning (0 - 30 s) as well as the end (50 - 100 s), but have lower quality results in between (30 - 50 s); the BP results from Away1 and Away2 arrays (Fig.4 (c) and (d)) are slightly more consistent with the slip-rate distribution within 30 - 50 s but give poorer constraint on the later stage of rupture after 50 s. During the first 30 s Toward and Away arrays exhibit quite similar results and have approximately the same level of CC values within both Sets (Fig.5 (a) and (b)).

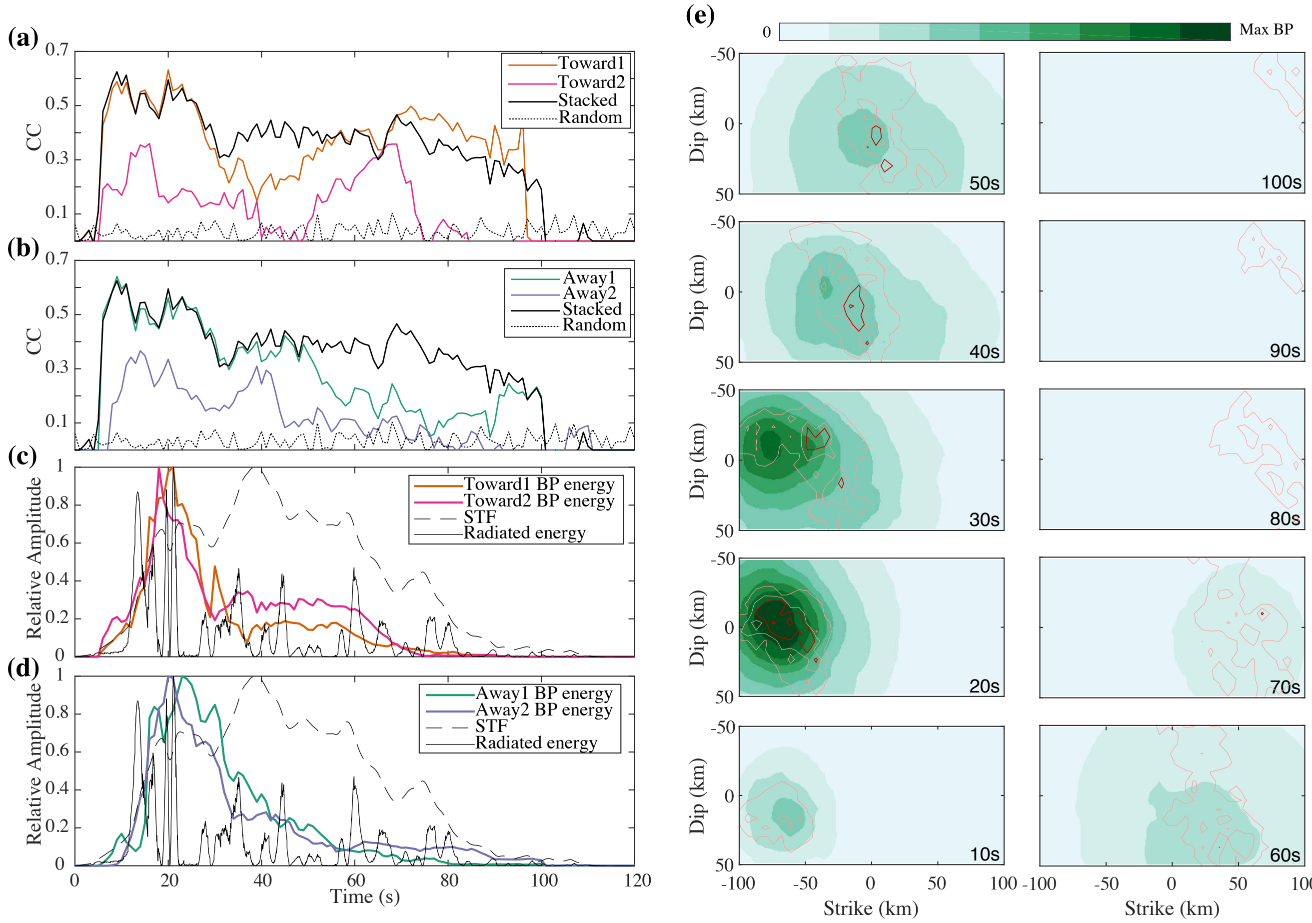

Figure 5. Comparison between the BP images and the kinematic source in the time domain: (a)-(b) the time-varying correlation coefficients (CC) between moment-rate distribution and BP images from all 4 different arrays (thin gray lines). The Toward1 and Toward2 arrays are color-highlighted in (a) while Away1 and Away2 arrays are highlighted in colors in (b). Bold black lines show the time-varying CC curve between moment-rate distribution and stacked BP results (also shown in (e)). The gray dashed line shows the correlation between moment-rate distribution and random images produced from uniform distribution. (c)-(d) show the normalized peak BP energy burst evolution from each array (Colored curves: Toward1 and Toward2 in (c) while Away1 and Away2 in (d)) comparing with the normalized source time function (STF, in gray dashed lines) and radiated energy evolution (squared time derivative of STF, in black lines). (e) Green images show the stacked BP images compared with slip rate distribution. Other symbols are the same as in Fig.4.

The complementary results obtained from the Toward and Away arrays imply that we can attempt to improve the BP results through stacking of seismic arrays. This stacking strategy has been successfully employed in previous studies (e.g., Zhang et al. 2016; Qin & Yao 2017). Based on Eq.(6), the stacking over various arrays is effectively a stack of their resolution matrix $\mathbf{F}(\omega)$ for the same source term $\dot{\mathbf{U}}(\omega)$ and thus improves the resolvability. We perform the stacking on the BP images from single array (Fig.4) to obtain the stacked results in Fig.5 (e). In practice, the stacking over different seismic arrays may require some weighting of the contributions of different arrays (Zhang et al. 2016). But in our synthetic test on stacking, the absolute amplitudes of BP images from each single array are preserved without extra weighting when stacking over arrays. This is reasonable because the aperture and scale of four synthetic arrays are similar but amplitude of waveforms varies a lot (Fig.2 (b)). Therefore, the direct stacking naturally allows the BP images from Set1 arrays with higher resolvability to dominate. As expected, the stacking can provide a sharper image and a better fit with stable CC from 0.4 to 0.6 (Fig.5 (a) and (b)) for the entire rupture duration.

Finally, it is common to analyze the temporal and spatial evolution of the peaks of the BP images. We can either look at

(i) the squared peak BP amplitudes, which is usually called relative energy radiation (Ishii et al. 2007), or (ii) track the spatial variation of BP peaks to estimate the rupture velocity.

(i) We compute the temporal evolution of the peak squared BP amplitude, that is, the relative energy radiation for each array (Fig.5 (c) and (d)). We also compare them with the squared moment acceleration (time derivative of source time function), which is proportional to the radiated energy (black lines in Fig.5 (c) and (d)). The BP peak amplitude from all arrays captures quite well the onset of the moment-rate and moment-acceleration functions, as also captured by the high CC values. Furthermore, the time series of BP energy resembles that of the squared moment acceleration. One possible explanation is the whitening of the BP spectrum during the stacking over frequency, which effectively brings up the level of the high frequencies. However, their strict similarity is hindered by methodological limitations such as off diagonal terms in the resolution matrix $\mathbf{F}(\omega)$, rupture directivity, even structural effects for the real BP applications.

(ii) Since the BP peaks are consistent with the peak locations of slip motion on the fault (Fig.S3 (a) in the Supplement), we can estimate the average rupture velocity from propagation of BP peaks. We use the BP results from the Away1 array (Fig.4 (c)) as an example. Similar to many BP studies (Meng et al. 2011; Yao et al. 2012; Wang et al. 2012; Yin et al. 2016, 2018), we estimate the average rupture velocity through a linear fit between the distance from epicenter to BP peaks and time (Fig.S3 (c) in the Supplement). We find that the rupture velocity estimated from the slip-rate peaks is 1.75 ± 0.03 km/s while the rupture velocity from BP peaks is 1.55 ± 0.06 km/s. The rupture velocity estimated from other arrays is generally consistent with slight difference (Toward1: 1.69 ± 0.09 km/s; Away2: 1.53 ± 0.08 km/s; Toward2: 1.62 ± 0.10 km/s).

4 RESOLVABILITY OF GLOBAL EARTHQUAKES AND ARRAYS

In addition to the synthetic exercise, our study aims to provide recommendations for BP studies through the evaluation of resolvability $\epsilon_I(\omega)$ given the global seismicity and accessible seismic networks. Based on Eqs.(4) and (5), we simply calculate $\mathbf{F}(\omega)$ with the radiation pattern terms R^P_{kn} and the relative position between global seismic stations and global source regions. We then use the Global Centroid Moment Tensor data base (GCMT, http://www.globalcmt.org/) to estimate the global seismicity radiation pattern (Fig.6)

In practice, the compilation of regional focal mechanisms of past moderate and large magnitude earthquakes allows us to construct an effective radiation pattern through averaging of strikes, dips, and rakes. We choose 19 regions in the world where the occurrence of large earthquakes ($M_w > 7.5$) is frequent (Fig.6). For each region we only select focal mechanisms from the $M_w > 7.5$ earthquakes with depth < 100 km and then directly average their source parameters: the 6 components of their moment tensor, longitude, latitude, and depth. We naturally weight the averages based on their seismic moment and let the focal mechanisms of the largest (M_w 8-9) dominate. Finally, we scale the seismic moment magnitude of these average earthquakes to be of M_w 8, above which BP method using teleseismic data works best (further discussion on this part in the later section).

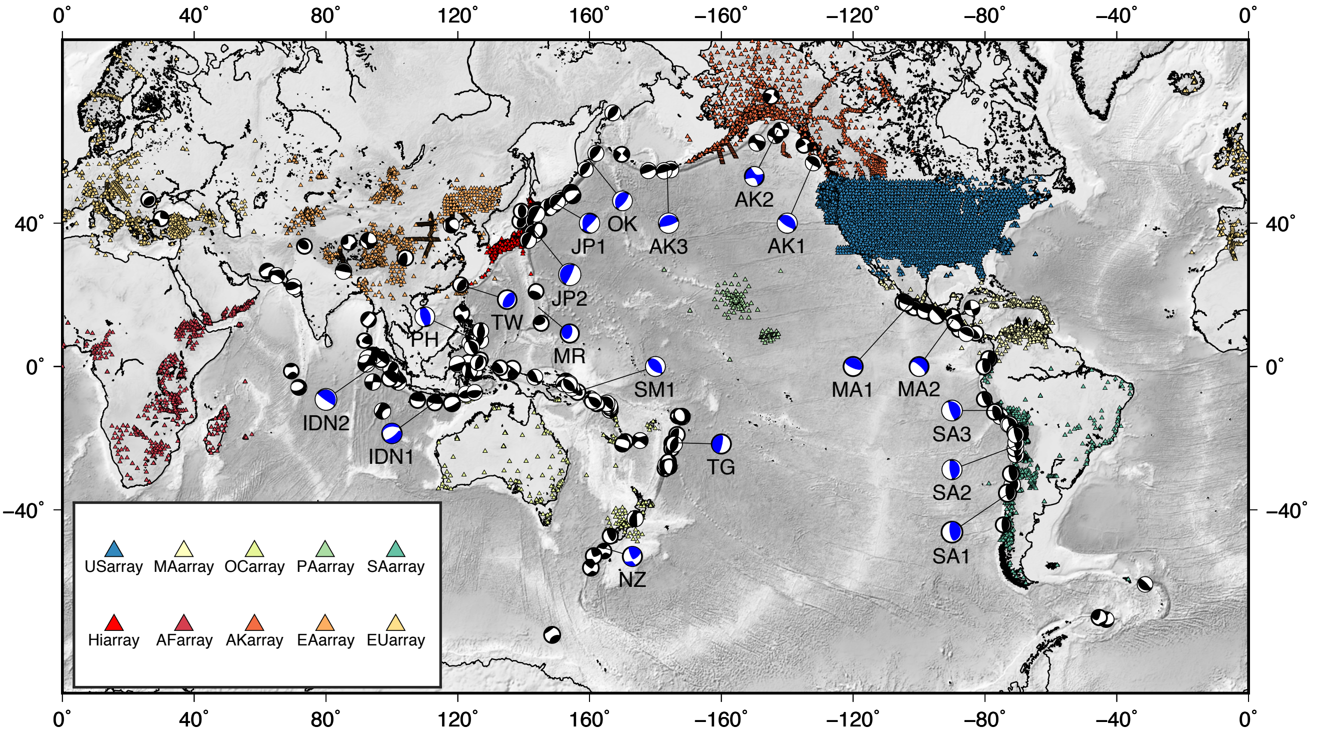

Figure 6. Global map of seismic arrays and focal mechanisms in this study. Colored triangles indicate various seismic arrays available since 2004 to 2018 on IRIS SeismicQuery website (https://ds.iris.edu/SeismiQuery/station.htm) and NIED Hi-net websites (http://www.hinet.bosai.go.jp/). Many of these stations may not be available/deployed during the same period of time. Black focal mechanisms are those of shallow (depth $<$ 100 km) earthquake with magnitude $M_w > 7.5$ from the Global Centroid Moment Tensor (GCMT) solution (http://www.globalcmt.org/). The average focal mechanism in each region is indicated by blue beach balls.

As for the distributions of the stations, we download the locations of all available stations from IRIS SeismicQuery website (https://ds.iris.edu/SeismiQuery/station.htm) and NIED Hi-net websites (http://www.hinet.bosai.go.jp/). Then, we cluster all these stations into large arrays. These arrays, including all temporary array stations, provide the ideal data coverage to apply the BP methods (Fig.6).

This study aims to provide an informed recommendation on the resolvability of the BP images given the source-receiver

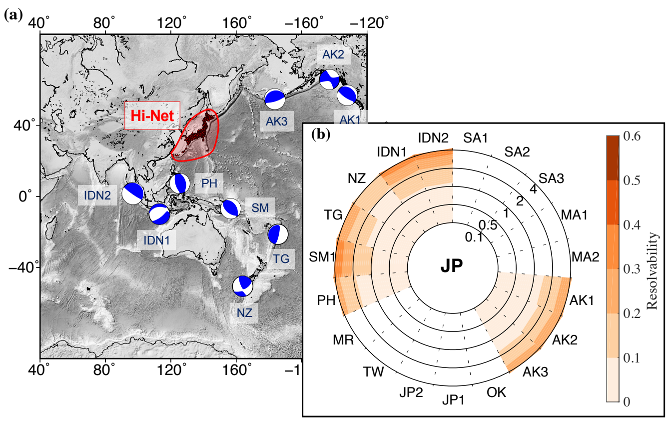

Figure 7. Resolvability of the Hi-Net array toward source regions within 30°-90° teleseismic distances. (a) Map view of the Hi-Net array and the averaged source focal mechanisms in each regions (blue beach balls). (b) The frequency-varying resolvability of Hi-Net array toward different regions. The concentric circles correspond to frequency from 0.1 Hz to 4 Hz in log scale. The resolvability is color-scaled in orange.

location. We first take the example of the Hi-net seismic array, a high quality dense seismic array (Okada et al. 2004; Obara et al. 2005; Ishii et al. 2005; Walker et al. 2005) and then provide a global perspective.

Fig.7 (a) shows an example of the seismic active regions within teleseismic distances ($30°$-$90°$) of the Hi-net array in Japan. The Hi-Net array can cover many major subduction zones including Indonesia (IDN1-Java and IDN2-Sumatra), Philippine (PH), Solomon (SM), Tonga (TG), and Alaska (AK1-Aleutian and AK3) subduction zones. In addition, there are also two transform plate boundaries in New Zealand (NZ) and Alaska (AK2). The average focal mechanisms shown in Fig.7 (a) are consistent with the geometry of the plate boundaries. We set the size of the potential source regions to be horizontal $4° \times 4°$ planes discretized with 32×32 grid points and choose the average depths of the M_w 7.5+ earthquake sources. Travel times from each grid point source to each station are computed using the IASP91 model (Kennett & Engdahl 1991). We then use Eqs.(4) and (5) to calculate the resolution matrix $\mathbf{F}(\omega)$ and the corresponding resolvability from Eq.(7). We focus on the frequency band from 0.1 to 4 Hz that is often used in backprojection studies. Fig.7 (b) shows the resolvability of the Hi-Net array toward all source regions. The resolvability is quite low below 1 Hz but rapidly improves at higher frequencies. Hi-net array can well resolve sources in Sumatra, Solomon, and Alaskan subduction zones. But it does not work well for the New Zealand (NZ) region because it is located too close to the nodal plane, which is the similar case as shown in our synthetic test results for the Set2 arrays.

We then show the resolvability distributions of all global seismic arrays in Fig.8. The systematic increase in resolvability with frequency is notable at all arrays and for all sources. Most of the large scale and dense arrays (USA (US), Eurasia (EA), Europe (EU), and Africa (AF)) have good resolvability to most source regions.

5 DISCUSSION

5.1 Using the linear BP image results to explain earthquake rupture

The theoretical formulation as well as the synthetic tests on complex kinematic sources help us to better interpret the BP images in light of earthquake kinematics. Since the displacement seismograms are determined mainly by integrating the slip-rate functions over the fault plane from Eqs.(1) and (2), the linear BP results constructed from the synthetic seismograms correspond well to the slip motions, i.e. the slip rates for displacement seismograms (this study) or slip accelerations for velocity seismograms. In the frequency domain, the BP image at each narrow frequency is actually consistent with the slip motion distribution filtered around that frequency (see Fig.S4 in the Supplement), consistent with on our theoretical formulation Eq.(6). However, in frequency domain BP, the displacement BP image and velocity BP image at the same frequency ω ought to be proportional $i\omega$.

As indicated in Fig.5 (a) and (b), for the four single arrays and the composite one, the average correlation coefficients between the average BP image and filtered slip-rate distribution generally varies between 0.1 to 0.6. This range of CC indicates

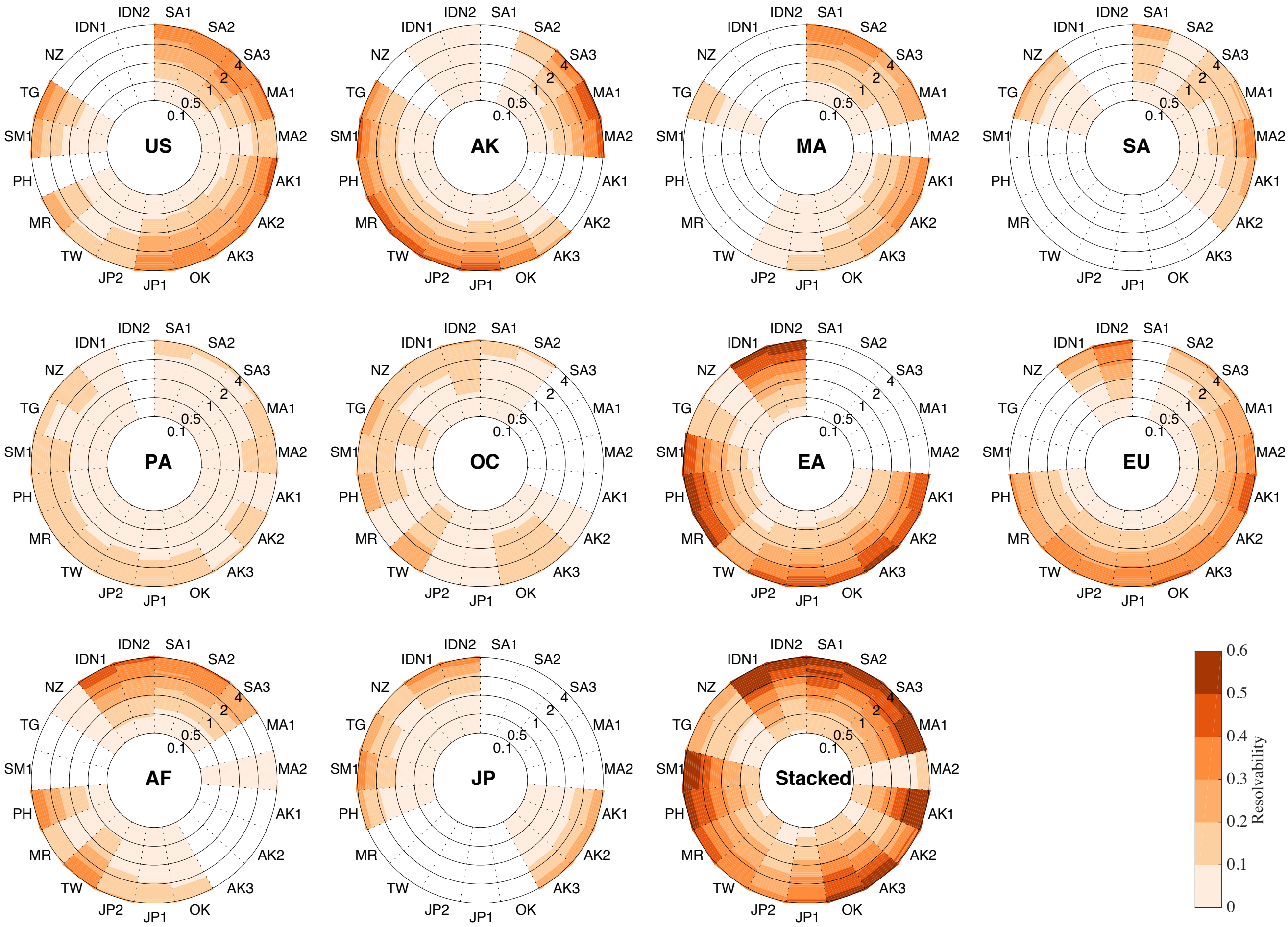

Figure 8. The same resolvability as Fig.7 (b) but for all global arrays. The location of arrays as well as the source regions can be found in Fig.6. The resolvability of all stacked array is shown in the bottom right.

that the BP method can recover relatively well the first order features of slip motion such as the slip peaks and spatial extent of rupture. The direct comparison between BP peaks and peak slip rates in Fig.S3 (a) can validate this consistency.

Since the peak slip rate always occurs slightly behind the true rupture front, our theoretical formulation and synthetic tests indicate that the BP image can give a good estimation on, at least, the lower limit of the average rupture velocity. In some specific cases, even the detailed changes of rupture velocity during an earthquake rupture can be possibly observed (e.g., Wang et al. 2012; Yin et al. 2018) given the good resolvability (Fig.8). Given the variations in rupture velocity that are estimated with the source-receiver geometry, we suggest that the rupture velocity obtained from BP studies is a robust lower limit estimation of the earthquake rupture velocity. On the other hand, the large variability of CC values (0.1-0.6) and lack of perfect value (CC=1) imply that the BP results cannot recover the exact slip history. We attribute this due to the shape of the resolution matrix $\mathbf{F}(\omega)$ that is not proportional to identity. A critical element of conventional BP is whether the waveforms can constructively or destructively interfere in the stacking. Low frequency waveforms have a wider sensitivity zone and are likely to interfere within a large source region (e.g. Fig.1 (a) and (d)), which further lowers the resolvability. On the other hand, the observed high-frequency data is limited due to attenuation and the non-stationary station coverage. This can be clearly quantified by the spectrum of BP resolvability. For instance, the resolvability of BP images constructed from the Hi-net stations of an earthquake in the Indonesia region (IDN1 or IDN2) increases from 0.1 at 0.1 Hz to 0.75 at 12 Hz (Supplement Fig.S5). However, seismic attenuation in the mantle constrains the upper observable teleseismic frequency to a maximum of 4 Hz, above which the signal-to-noise ratio of teleseismic seismograms is very low (e.g., Warren & Shearer 2000, 2002).

Therefore, we conclude that the BP images derived from raw seismic data, if corrected for attenuation, are proportional to the slip-rate field after a spatial smoothing, which can be parameterized by the resolution matrix $\mathbf{F}(\omega)$ (Fig.1). This is similar to the conclusions of Fukahata et al. (2014) that the BP image represents the slip motion on a fault, provided that the Green's function is sufficiently close to a delta function. Our results, however, show that the Green's function cannot realistically be a delta function, but that general features of the slip motions may be recovered within limited frequency bandwidth.

The relation between the BP image and the kinematic source process provides a unique way to infer the slip behaviors in the relatively higher BP frequency band: the high frequency components of the slip history, parameterized either with slip rate or acceleration, are sensitive to the sudden change of rupture propagation (Madariaga 1977, 1983) and thus can be used to estimate the overall pattern of rupture propagation such as the rupture extend or lower limit of rupture velocity.

Many previous studies on the megathrust events reveal a frequency-depth relation of the seismic radiation coherence in the BP results (e.g., Wang & Mori 2011; Lay et al. 2012; Sufri et al. 2012; Yao et al. 2013; Melgar et al. 2016; Yin et al. 2016). Interestingly, this pattern cannot be clearly observed in our synthetic kinematic sources: neither in the filtered slip motion distribution nor in the BP images (see Fig.S4 in the Supplement). This implies that the occurrence of frequency-dependent seismic radiation may require additional source heterogeneities that would cause systematic spatial variations of rise times or slip-rate functional forms, but that are not modeled in our kinematic source. These heterogeneities may be better modeled with realistic dynamic models that account for pre-stress (Huang et al. 2012), friction (Rice 1993; Scholz 1998), fault geometry (Madariaga et al. 2006) or even inelasticity effects (Ma & Hirakawa 2013) along dip direction,not included in this study but worth further investigations.

Finally, we discuss the spectral decay of the BP amplitudes. At any time, the BP amplitude decays with frequency in a way that is similar to the source spectral decay (Fig.S6 in the Supplement). The high frequency spectral falloff rate of this BP peak amplitude spectrum from linear regression varies from 2.9 to 3.3 for all four arrays in our synthetic tests with kinematic source (Fig.S6 in the Supplement). Considering the spectral falloff rate of the sliding time window, which is 1 for the Tukey taper used in this study, the corrected source spectral falloff rate estimated from BP peak amplitude can be 1.9 to 2.3 in 0.1-1 Hz. The falloff rates of BP peak amplitude spectra are roughly consistent with the spectral falloff rates of the sources, 2.2 (Fig.S1 in the Supplement) for the kinematic model. In practice and for further interpretation of the spectral decay in terms of rupture process, a correction of the amplitude for high frequency attenuation is required and remains challenging.

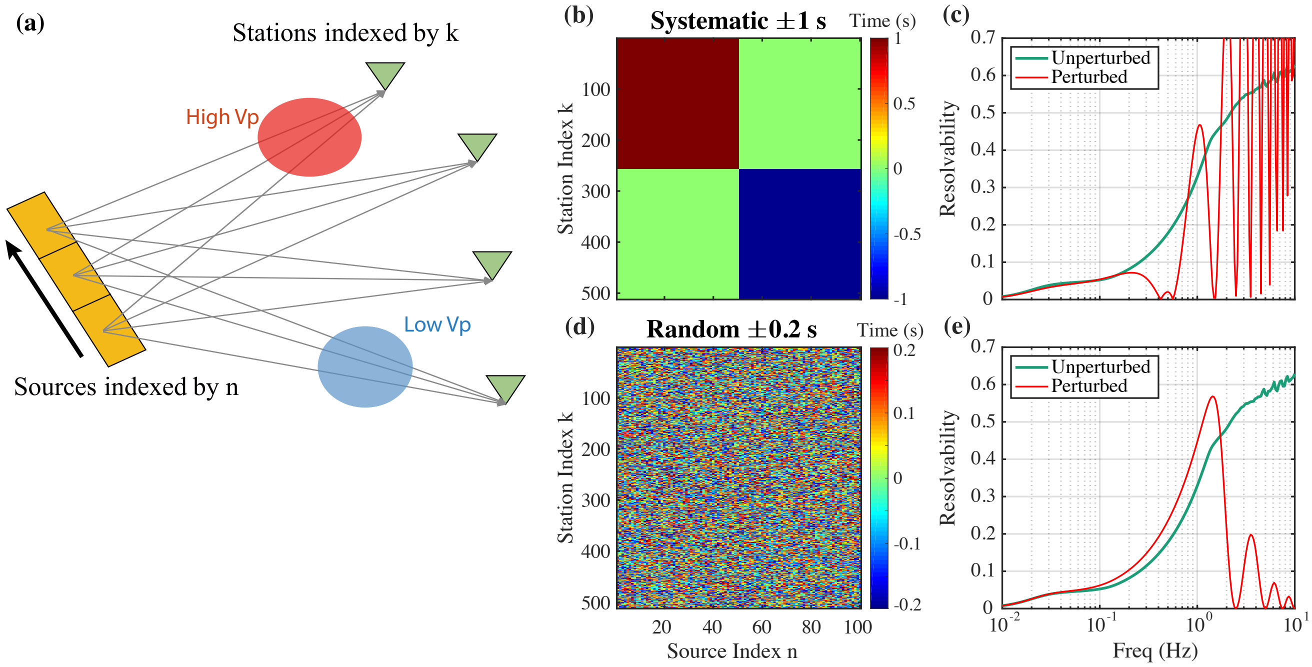

Figure 9. Generalized resolvability with travel time perturbation. (a) A schematic cartoon shows the structural heterogeneities along the ray path. The yellow rectangle is a source with 3 grids indexed by n. Black arrow shows the rupture propagation. Green triangles are the stations indexed by k. The two circle patches show the velocity anomalies along the ray paths from each source grid to stations. (b)-(c) The systematic travel-time perturbation matrix Δt^1_{kn} and its corresponding resolvability, respectively. (d)-(e) The random travel-time perturbation matrix Δt^2_{kn} and its corresponding resolvability, respectively. In (c) and (f) the green lines are the Away1 array resolvability, the same as shown in Fig.3 (c) and the red lines are the corresponding resolvability from travel time perturbations.

5.2 Discussion on 3D structural effects on resolvability $\epsilon_I(\omega)$

In this study, the theoretical relation of Eq.(6) is described in a homogeneous full space and so we assume an ideal case that we can perfectly correct the travel time: the travel-time terms in the matrices $\tilde{\mathbf{A}}(\omega)$ and $\mathbf{A}(\omega)$ are equal. Under this assumption, we have ignored the uncertainty of the travel-time corrections that may present in practice. While both source and path complexity affect the seismograms, our primary motivation of this study is to map the source complexity with idealized path terms. In this section, we briefly address the impact of path complexity on resolvability. The concept of BP resolvability $\epsilon_I(\omega)$ is to propose an upper bound of our confidence in the BP images, i.e., to what extend we can recover the source kinematics from BP images.

A first element we can incorporate is a variable contributions of stations and arrays. For example, the relation of Eq.(6) ignores the weighting matrix $\mathbf{W}$. We can generalize the resolution matrix $\mathbf{F}^g(\omega) = \tilde{\mathbf{A}}(\omega)\mathbf{W}\mathbf{A}(\omega)$ to account for the waveform normalization, different array contributions and polarity reversal.

A second element we can incorporate is travel-time uncertainty due to the unknown 3D structure. In realistic situation, the travel-time terms in the wave propagation matrix $\mathbf{A}(\omega)$ and the BP phase shift matrix $\tilde{\mathbf{A}}(\omega)$ are different: in the former the t_{kn} is the true travel time while in the latter t_{kn} is a theoretical estimate. To account for this difference, we note $\tilde{\mathbf{A}}(\omega)$ to be t'_{kn} as the theoretical travel time and regard the t_{kn} in $\mathbf{A}(\omega)$ as the true travel time. For example, the diagonal phase-shift terms now become $F_{nn}(\omega) = \sum_k \frac{R^P_{kn}}{r_{kn}} e^{i\omega(t'_{kn} - t_{kn})}$. Then, we can model uncertainties in travel time due to our limited knowledge of the Earth structure, in particular for small length-scale anomalies rays travel through.

To simulate these effects on the BP resolution, we design two different kinds of travel time perturbations, one that is far-field systematic shift, one that is typical of local site effects (Fig.9 (a)). We use the synthetic setting of Away1 array as an example. We add the travel-time perturbations as $\Delta t_{kn} = t'_{kn} - t_{kn}$, re-construct $\mathbf{F}(\omega)$ as well as the resolvability. The first uncertainty Δt^1_{kn} is a systematic travel-time shift of ± 1 s added to half of the source-receiver pair (-1s for 1/4 and +1s for the other 1/4, see Fig.9 (b)). The second kind of perturbation Δt^2_{kn} is a simple random shift taken from a uniform distribution with maximum amplitude of 0.2 s (Fig.9 (d)).

Both types of uncertainty impact the resolvability. The systematic perturbation causes significant fluctuations in the resolvability (Fig.9 (c)): the resolvability drops at specific frequencies. Because these time shifts act as waveform re-alignment, it is likely that the alignment and stacking produce spurious arrivals, shifted by the uncertainty that interfere constructively or destructively at the specific frequencies harmonic to the inverse of the uncertainty phase shift. Intuitively, it is similar to taking the Fourier transform of a time series with two pulses (e.g., Denolle et al. 2015). This large effect in the resolvability yields a systematic location bias in the BP images (Supplements Fig.S7 (b) and (e)). On the other hand, the random perturbation has little effect on the resolvability at low frequency and even provides even a higher resolvability (Fig.9 (e)). This is because the incoherent part of waveforms can be better destructively stacked after adding this random perturbation. The random perturbation becomes rough but also slightly "sharpens" the edge of BP images (Supplements Fig.S7 (c) and (f)), thus leads to relatively higher resolvability. However, it causes a steep decrease of the resolvability at the high frequency, indicating a severe lost of waveform coherency and poor resolution on the short-wavelength features.

Our tests confirm that travel-time uncertainty can greatly influence the resolution in BP images. Besides, these tests also suggest a high frequency cutoff of applicability of the BP techniques of 2 Hz in this test, given a 0.2 s travel-time uncertainty. This factor, together with the structural attenuation, poses a upper limits on the frequency of BP technique. In real applications, many efforts have been devoted to better corrections on structural effects, using theoretical or empirical methods(e.g., Ishii et al. 2007; Meng et al. 2016, 2018).

A third element present in 3D structure are the near-source body-wave reflections such as depth phases (Langston 1978; Warren & Shearer 2005; Denolle et al. 2015; Yin et al. 2018) and water reverberation (Chu et al. 2011; Akuhara & Mochizuki 2015; Yue et al. 2017) that are particularly visible in megathrust events. It is possible to include these phases in a more generalized wave propagation matrix $\mathbf{A}^g(\omega)$ as a linear summation of the phases (e.g., see Eq.(6) in Yin et al. 2018):

$$\mathbf{A}^g(\omega) = \mathbf{A}^P(\omega) + \mathbf{A}^{pP}(\omega) + \mathbf{A}^{sP}(\omega) + ... \tag{10}$$

Then the corresponding BP phase-shift matrix would be:

$$\tilde{\mathbf{A}}^g(\omega) = \tilde{\mathbf{A}}^P(\omega) + \tilde{\mathbf{A}}^{pP}(\omega) + \tilde{\mathbf{A}}^{sP}(\omega) + ... \tag{11}$$

Interferences and coherence among depth phases will appear in the generalized resolution matrix as the product of the these summed matrices. The arrival times of depth phases and water reverberation are source-specific and a rather systematic parameter space study of these effects are left for future work. Nonetheless, this scheme is theoretically simple and may be useful in the future to better evaluate how BP can work under the more realistic conditions.

5.3 Relation to other improved BP techniques

The relation shown in Eq.(6) provides a fundamental framework between BP images and slip-rate field, provided that the stacking scheme is linear. This well motivated our work and also has been emphasized in previous studies (e.g., Kiser & Ishii 2017). Sophistication of the data processing that looses the linearity in Eq.(6) is attempting to improve image resolution: for instance, the use of sparsity regularization (Compressive Sensing (CSBP), Yao et al. 2011; Yin & Yao 2016; Yin et al. 2018), hybrid backprojection (HyBP, Yagi et al. 2012; Fukahata et al. 2014) and the n^{th} root stacking processing (e.g., Rost & Thomas 2002; Xu et al. 2009; Meng et al. 2011).

Inspired by techniques developed in signal processing and applied mathematics communities, Yao et al. (2011) develops a compressive sensing BP method, CSBP, to invert for a sparse distribution of the source $\dot{\mathbf{U}}(\omega)$ (or $\ddot{\mathbf{U}}(\omega)$ from velocity seismograms) in Eq.(3). Since this system is under-determined ($K \ll N$), we cannot get a unique solution without smoothing constraints. The basic assumption of CSBP is that the source distribution is sparse in space so the problem is solved via optimization,

$$\mathbf{U}^{CS}(\omega) = argmin\{\|\mathbf{D}(\omega) - \mathbf{A}(\omega)\mathbf{U}(\omega)\|_{1or2} + \lambda\|\mathbf{U}(\omega)\|_1\}, \tag{12}$$

where λ is a damping factor chosen to balance the contributions of data misfit (first term in right hand side) and model constraint (second term in right hand side). Instead of directly aligning and stacking in a sense of "grid-search" like conventional BP, CSBP is based on an inversion scheme that attempts to directly solve for the source $\mathbf{U}(\omega)$ with the specific constraint of sparsity. The advantage of sparsity constraint is its relatively high spatial resolution. The sparsity constraint helps to accurately locate the sub-events, especially when limited by lower seismic frequencies. Ignoring the damping required to balance data and model misfit, the CSBP is equivalent to the sparse solution of $\mathbf{U}^{BP}(\omega)$ in Eq.(6), constrained by the data. The sparse representation inevitably eliminates details about the source but can provide more robust locations of the dominant sources. This latter effect is practical when the spatial resolution of conventional BP method is relatively poor (see Fig.S8). Similarly, we can also look at the CSBP peaks and estimate the average rupture velocity (see Fig.S3 (b) and (d) in the Supplement for instance). Overall, CSBP provides a sparse fit to the slip-rate field.

The Hybrid BP technique (HyBP, Yagi et al. 2012) is another improved BP technique that can be clearly discussed under the framework in this study. In our study, the alignment of the waveform, $\tilde{\mathbf{A}}(\omega)$, is carried by simplifying the Green's function to a shifted delta function, that is, directly time/phase shifting without changing waveforms. The HyBP, however, incorporates the full Green's function in $\mathbf{A}^{thG}(\omega)$, as a combination of slip inversion with conventional BP techniques. The basic assumptions are that the cross-correlation between the theoretical Green's function and real Green's function can be approximated to the auto-correlation of real Green's function, and that it is sufficiently close to a delta function (Fukahata et al. 2014). If these assumptions are satisfied, the cross-correlation function can directly reflect the slip motion occurring at the source thus we can use the HyBP to directly recover the slip motion. The calculation of the cross-correlation function is equivalent to multiplying a $N \times K$ cross-correlation matrix $\mathbf{A}^{thG}(\omega)$ to the left-hand side side of Eq.(3):

$$\mathbf{A}^{thG}(\omega)\mathbf{D}(\omega) = \mathbf{A}^{thG}(\omega)\mathbf{A}(\omega)\mathbf{U}(\omega). \tag{13}$$

The elements of $\mathbf{A}^{thG}(\omega)$ are:

$$(\mathbf{A}^{thG}(\omega))_{nk} = C_{nk}\frac{R^P_{kn}}{r_{kn}}e^{+i\omega t_{kn}}, \tag{14}$$

where C_{nk} is a normalization constant for the cross correlation and the subscripts $k = 1, 2, ..., K$ and $n = 1, 2, ..., N$ correspond to the station and source index for the theoretical Green's function, respectively; other terms have the same notation as in Eqs.(1)-(4). Compared with Eqs.(4) and (5), the HyBP method effectively consists of the multiplication $\mathbf{A}^{thG}(\omega) = \mathbf{A}^{\mathbf{H}}(\omega)$, the conjugate transpose of $\mathbf{A}(\omega)$ to the spectral data, and forms a new resolution matrix $\mathbf{F}^{\mathbf{HyBP}}(\omega) = \mathbf{A}^{\mathbf{H}}(\omega)\mathbf{A}(\omega)$. Based on our theoretical formulation Eqs.(4)-(5) and (13)-(14), the HyBP method is the same as Linear BP in the frequency domain, except for its resolution matrix $\mathbf{F}^{\mathbf{HyBP}}(\omega)$. Both methods can be interpreted as cross-correlation: linear BP is the result from cross-correlation with a phase-shifted delta function $\delta(t - t_{kn})$ while the HyBP is the outcome from cross-correlation with the theoretical Green's function. The difference in the BP results due to their respective resolution matrices is negligible (Supplement Fig.S9). In practice, the cross-correlation with an accurate Green's function can potentially suppress incoherent noise and thus enhance the signal levels of the source waveforms. However, basic assumptions of HyBP are difficult to satisfy: (i) accurate theoretical Green's functions are difficult to compute due to limited knowledge of structure and computation cost of high frequency wave propagation; (ii) even the theoretical Green's function is equal to real Green's function, the auto-correlation of a Green's function is not exactly a delta function due to finite-frequency effects. Therefore, the BP images from HyBP are still not the perfect match to slip motion on the fault surface.

Finally, we briefly discuss the popular non-linear stacking schemes. n^{th} root stacking (e.g., Rost & Thomas 2002; Xu et al. 2009; Meng et al. 2011) is another classical beamforming technique. It first calculates the n^{th} root (n=2,3,4,...) of the seismogram in Eq.(1) before stacking. This power-law processing removes the linearity between slip-rate and displacement waveforms, and thus we have already lost the information about the slip motion in the data. However, it is practical to enhance phase coherency (Rost & Thomas 2002) and thus to provide better resolution of radiation locations. To sum up, the n^{th} root stacking can definitely improve the resolution of BP image but in order to keep the slip information about the source (dimension of slip motions), linear stacking is necessary.

5.4 Global array stacking and frequency resolution

Nowadays, there are several available seismic arrays within the teleseismic distance of a given earthquake. This allows us to combine multiple arrays and improve the array response and resolution of BP method. The BP stacking over multiple arrays has

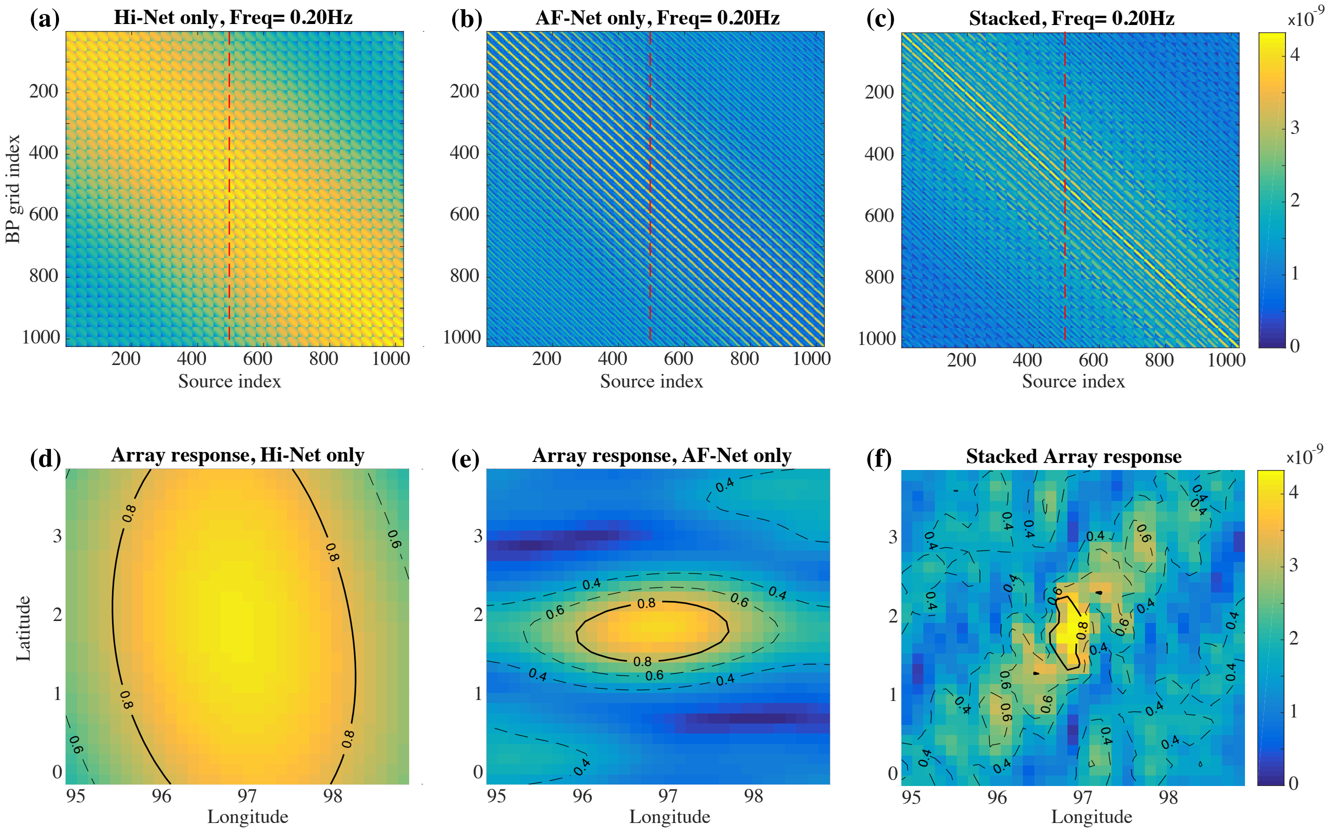

Figure 10. Example of array response varying with array locations and the improvement from array stacking at a given seismic frequency. Absolute value of resolution matrices of Hi-Net (a) and AF arrays (b) toward the region IDN2 at 0.2 Hz. Array responses at a point source location corresponding to Hi-Net (c) and AF (d) arrays. Absolute value of stacked resolution matrix from all available arrays within teleseismic distance to the region IDN2 (AK, OC, EA, EU, AF, JP) (e) and the corresponding array response at the same source location (f). Areas within the 0.8 contours of array response distribution will be used to estimate the resolvable areas of Fig.11.

been applied in various recent studies (e.g., Zhang et al. 2016; Qin & Yao 2017). Here, we relate the multiple arrays stacking to our theoretical formulation and indicate how well it improves the BP results.

The shape of resolution matrix itself carries information about the data resolution given a source-receiver geometry. Each column of $\mathbf{F}(\omega)$ corresponds to the array response (Rost & Thomas 2002; Xu et al. 2009) of a seismic array toward a single grid point source at a specific seismic frequency. The array response is determined by both the azimuth and distance coverage (Kiser & Ishii 2017), and a wide azimuth-distance coverage lead to the different distributions of array response.

For example, Fig.10 shows the resolution matrices of Hi-Net and AF-Net arrays as well as their array responses at 0.2 Hz for the IDN2 region, where the 2004 Sumatra earthquake occurred. Ishii et al. (2005) use the Hi-net array to recover the rupture process of this event. However, the array response of Hi-net array shows a north-south distributed patch (Fig.10 (d)) and the size of this patch is very large due to the limited coverage of Hi-net array. On the other hand, if there had been enough high quality stations in Africa, the corresponding array response at the same point is east-westward distributed with smaller size (Fig.10 (e)) due to better spatial coverage. Moreover, the resolution matrices of these two arrays are different at most locations but both have peak values at the diagonal parts of the resolution matrix (Fig.10 (a) and (b)). This is actually the basis of the multiple-array stacking that can improve the convergence of the resolution matrix to a diagonal matrix. For the IDN2 region,

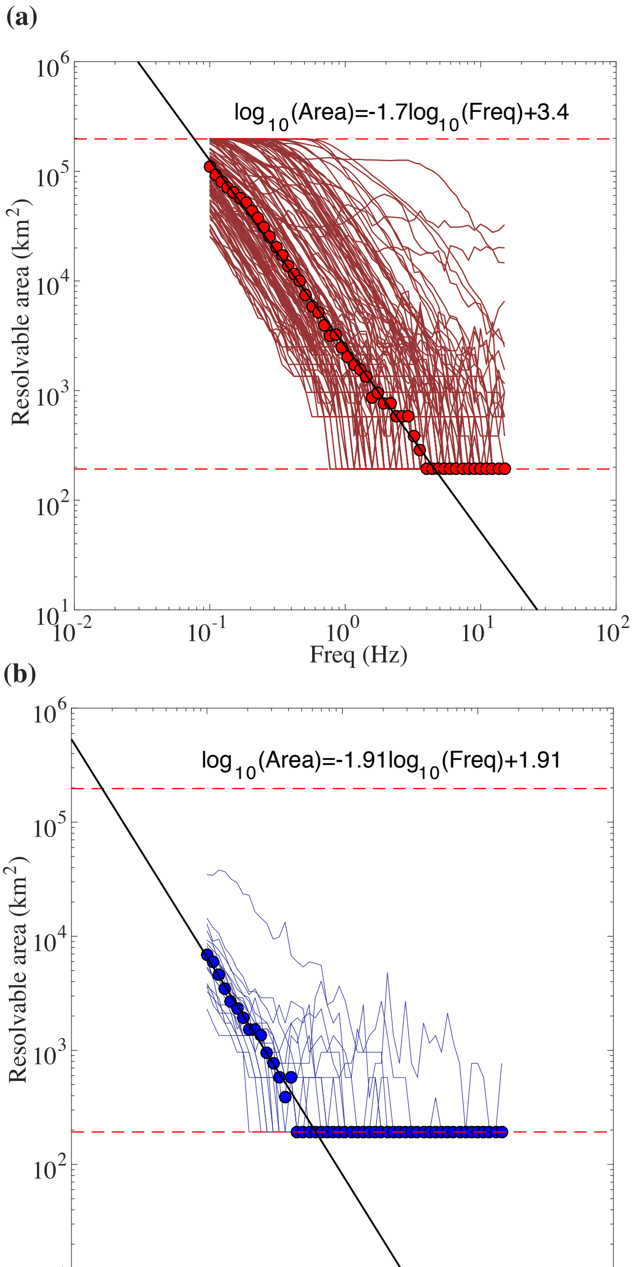

Figure 11. Resolvable area as a function of frequency. Red dashed lines corresponds to the minimum (grid size) and maximum (total) area of the source region. (a) Thin red curves show the frequency-varying resolvable area from each array-source region pair. Red circles corresponds to the median value of resolvable area at each frequency. Black line shows the relation between median resolvable area and frequency from linear regression. (b) Blue curves show the variation of the resolvable area as a function of seismic frequency from multiple-array-stacking for each source region. Blue circles corresponds to the median value of the stacked resolvable area at each frequency. The black line shows the best-fit relation from linear regression to the median values.

we stack the resolution matrices of all the available arrays (JP (Hi-Net), AF, OC, AK, EA, EU arrays). The resolvability is greatly improved (Fig.10 (c) and (f)), even at low frequency. For all other regions, the improvements of resolvability are all obvious (last sub-figure in Fig.8).

For each array response matrix, i.e. for each source-array configuration, and at each seismic frequency, we attribute as resolvable area as the integrated area within 80% of the peak array response function (Fig.1 (d)-(f) and Fig.10 (d)-(f)). For all source-array configurations and at all frequencies, we construct an empirical relation between the spatial resolution and the frequency of the data. All available configurations are shown in Fig.11 (a) and exhibit unique levels of resolvability, whereby the resolvable area decreases with seismic frequency, and equivalently, spatial resolution increases. By taking the median of individual area measurement at each frequency, we construct an empirical relation between the BP resolvable area $S_0^{\mathbf{BP}}$ (in km^2) and seismic frequency f (in Hz) as a power law of seismic frequency:

$$S_0^{\mathbf{BP}} \approx 10^{3.4} f^{-1.7}. \tag{15}$$

In the ideal case that each source region can be well recorded by all available arrays, we proceed by stacking over arrays to increase resolvability (Fig 11 (b)). The optimal median resolvable area $S^{\mathbf{BP}}$ - seismic frequency f is:

$$S^{\mathbf{BP}} \approx 10^{1.91} f^{-1.91}. \tag{16}$$

An additional practical consideration is that of earthquake size scaling. If the fault length is $L = (S^{\mathbf{BP}})^{1/2}$, then $L \approx 10/f \approx 2V_P/f = 2\lambda_P$. That is, our empirical relation implies a twice P wavelength resolution for the BP. Given scaling between fault length and earthquake magnitude M_w provided by (Table 2A, Wells & Coppersmith 1994),

$$S \approx 10^{(-3.42+0.9M_w)}. \tag{17}$$

In order to resolve the rupture propagation, the BP resolvable area $S^{\mathbf{BP}}$ should be smaller than the total rupture area. For example, if $S^{\mathbf{BP}} \leq S/10$ is required, we can build a relation between earthquake magnitude and lowest BP frequency f_{min}^{BP} required to resolve source features:

$$f_{min}^{BP} \approx 10^{(3.31-0.47M_w)}. \tag{18}$$

In order to resolve the source features of a M_w 8 earthquake using multiple-array BP, the lowest seismic frequency required is approximately 0.35 Hz; 1.02 Hz for a M_w 7, and 3.02 Hz for a M_w 6 earthquake. Because the relation Eq.(17) between rupture area and earthquake magnitude from Wells & Coppersmith (1994) is mostly from continental earthquakes, the actual rupture area of megathrust events in the subduction zones can be larger. Therefore, the corresponding lowest BP frequency can be smaller than the value predicted from Eq.(18) when BP is applied to the megathrust events.

This purely empirical relation only provides crude guidelines on the lower bound of the BP frequency analysis. Further considerations such as attenuation, structure, signal levels will impact the upper bound frequency.

6 CONCLUSION

Our theoretical formulation of the linear backprojection algorithm indicates that the BP image is indeed related to the slip motion on the fault, granted a spatial smoothing. A resolvability parameter, which we defined as the norm of the resolution matrix, provides a metric to evaluate the spatial resolution of backprojection method for a specific source-receiver geometry.

We further test the BP method on a synthetic kinematic source to validate the theoretical formulation. The synthetic tests indicate that the BP image can provide a reliable estimation on the general pattern of rupture propagation.

In addition, we estimate the strengths and limitations of the linear BP algorithm in light of realistic source and seismic array configurations. We find that stacking arrays considerably increases the resolution thereby reducing the resolvable area. Finally, we construct a relation between resolvable area and seismic frequencies. Given the scaling of earthquake size with source length, our analysis provide simple guidelines to the lower bounds of seismic frequencies required to image details of the source provided earthquake magnitude.

ACKNOWLEDGMENTS

The authors sincerely thank Dun Wang and Ryo Okuwaki for their constructive comments and advices on the manuscript. The authors also appreciate the helpful comments from the two anonymous reviewers to greatly improve the manuscript. Station information is obtained from IRIS SeismiQuery website (https://ds.iris.edu/SeismiQuery/station.htm) and NIED Hi-net official website (http://www.hinet.bosai.go.jp/). Focal mechanisms of historical earthquakes are downloaded from GCMT website (http://www.globalcmt.org/). Most of the data processing, calculations and figures are carried out using Matlab and some map figures are made using GMT (the Generic Mapping Tools, http://gmt.soest.hawaii. edu/projects/gmt/wiki/Download).

References

Aki, K. & Richards, P. G., 2002. *Quantitative Seismology, 2nd Ed.*.

Akuhara, T. & Mochizuki, K., 2015. Hydrous state of the subducting Philippine Sea plate inferred from receiver function image using onshore and offshore data, *Journal of Geophysical Research: Solid Earth*, **120**(12), 2015JB012336.

Avouac, J.-P., Meng, L., Wei, S., Wang, T., & Ampuero, J.-P., 2015. Lower edge of locked Main Himalayan Thrust unzipped by the 2015 Gorkha earthquake, *Nature Geoscience*, **8**(9), 708–711.

Burridge, R. & Knopoff, L., 1964. Body force equivalents for seismic dislocations, *Bulletin of the Seismological Society of America*, **54**(6A), 1875–1888.

Campillo, M. & Paul, A., 2003. Long-Range Correlations in the Diffuse Seismic Coda, *Science*, **299**(5606), 547–549.

Chu, R., Wei, S., Helmberger, D. V., Zhan, Z., Zhu, L., & Kanamori, H., 2011. Initiation of the great M w 9.0 TohokuOki earthquake, *Earth and Planetary Science Letters*, **308**(3), 277–283.

Crempien, J. G. F. & Archuleta, R. J., 2014. UCSB Method for Simulation of Broadband Ground Motion from Kinematic Earthquake Sources, *Seismological Research Letters*.

Denolle, M. A., Fan, W., & Shearer, P. M., 2015. Dynamics of the 2015 M7.8 Nepal earthquake, *Geophysical Research Letters*, **42**(18), 2015GL065336.

DMC, I., 2011. Data Services Products: BackProjection P-wave back-projection rupture imaging.

Duputel, Z. & Rivera, L., 2017. Long-period analysis of the 2016 Kaikoura earthquake, *Physics of the Earth and Planetary Interiors*, **265**, 62–66.

Eberhart-Phillips, D., Haeussler, P. J., Freymueller, J. T., Frankel, A. D., Rubin, C. M., Craw, P., Ratchkovski, N. A., Anderson, G., Carver, G. A., Crone, A. J., Dawson, T. E., Fletcher, H., Hansen, R., Harp, E. L., Harris, R. A., Hill, D. P., Hreinsdttir, S., Jibson, R. W., Jones, L. M., Kayen, R., Keefer, D. K., Larsen, C. F., Moran, S. C., Personius, S. F., Plafker, G., Sherrod, B., Sieh, K., Sitar, N., & Wallace, W. K., 2003. The 2002 Denali Fault Earthquake, Alaska: A Large Magnitude, Slip-Partitioned Event, *Science*, **300**(5622), 1113–1118.

Fan, W. & Shearer, P. M., 2015. Detailed rupture imaging of the 25 April 2015 Nepal earthquake using teleseismic P waves, *Geophysical Research Letters*, **42**(14), 2015GL064587.

Frankel, A., 2009. A Constant Stress-Drop Model for Producing Broadband Synthetic Seismograms: Comparison with the Next Generation Attenuation RelationsConstant Stress-Drop Model for Producing Broadband Synthetic Seismograms, *Bulletin of the Seismological Society of America*, **99**(2A), 664–680.

Fukahata, Y., Yagi, Y., & Rivera, L., 2014. Theoretical relationship between back-projection imaging and classical linear inverse solutions, *Geophysical Journal International*, **196**(1), 552–559.

Huang, Y., Meng, L., & Ampuero, J.-P., 2012. A dynamic model of the frequency-dependent rupture process of the 2011 Tohoku-Oki earthquake, *Earth, Planets and Space*, **64**(12), 1.

Ishii, M., Shearer, P. M., Houston, H., & Vidale, J. E., 2005. Extent, duration and speed of the 2004 SumatraAndaman earthquake imaged by the Hi-Net array, *Nature*, **435**(7044), 933.

Ishii, M., Shearer, P. M., Houston, H., & Vidale, J. E., 2007. Teleseismic P wave imaging of the 26 December 2004 Sumatra-Andaman and 28 March 2005 Sumatra earthquake ruptures using the Hi-net array, *Journal of Geophysical Research: Solid Earth*, **112**(B11), B11307.

Ji, C., Wald, D. J., & Helmberger, D. V., 2002a. Source Description of the 1999 Hector Mine, California, Earthquake, Part II: Complexity of Slip History, *Bulletin of the Seismological Society of America*, **92**(4), 1208–1226.

Ji, C., Wald, D. J., & Helmberger, D. V., 2002b. Source Description of the 1999 Hector Mine, California, Earthquake, Part I: Wavelet Domain Inversion Theory and Resolution Analysis, *Bulletin of the Seismological Society of America*, **92**(4), 1192–1207.

Kennett, B. L. N. & Engdahl, E. R., 1991. Traveltimes for global earthquake location and phase identification, *Geophysical Journal International*, **105**(2), 429–465.

Kikuchi, M. & Kanamori, H., 1982. Inversion of complex body waves, *Bulletin of the Seismological Society of America*, **72**(2), 491–506.

Kiser, E. & Ishii, M., 2017. Back-Projection Imaging of Earthquakes, *Annual Review of Earth and Planetary Sciences*, **45**(1), 271–299.

Kiser, E., Ishii, M., Langmuir, C. H., Shearer, P. M., & Hirose, H., 2011. Insights into the mechanism of intermediate-depth earthquakes from source properties as imaged by back projection of multiple seismic phases, *Journal of Geophysical Research: Solid Earth*, **116**(B6), B06310.

Koper, K. D., Hutko, A. R., Lay, T., Ammon, C. J., & Kanamori, H., 2011. Frequency-dependent rupture process of the 2011 M w 9.0 Tohoku Earthquake: Comparison of short-period P wave backprojection images and broadband seismic rupture models, *Earth, planets and space*, **63**(7), 599–602.

Langston, C. A., 1978. Moments, corner frequencies, and the free surface, *Journal of Geophysical Research: Solid Earth*, **83**(B7), 3422–3426.

Lay, T., Kanamori, H., Ammon, C. J., Koper, K. D., Hutko, A. R., Ye, L., Yue, H., & Rushing, T. M., 2012. Depth-varying rupture properties of subduction zone megathrust faults, *Journal of Geophysical Research: Solid Earth*, **117**(B4), B04311.

Liu, P., Archuleta, R. J., & Hartzell, S. H., 2006. Prediction of Broadband Ground-Motion Time Histories: Hybrid Low/High- Frequency Method with Correlated Random Source Parameters, *Bulletin of the Seismological Society of America*, **96**(6), 2118–2130.

Ma, S. & Hirakawa, E. T., 2013. Dynamic wedge failure reveals anomalous energy radiation of shallow subduction earthquakes, *Earth and Planetary Science Letters*, **375**, 113–122.

Madariaga, R., 1977. High-frequency radiation from crack (stress drop) models of earthquake faulting, *Geophysical Journal International*, **51**(3), 625–651.

Madariaga, R., 1983. High frequency radiation from dynamic earthquake fault models, *Annales de Geophysique*, **1**(1), 17–23.

Madariaga, R., Ampuero, J. P., & Adda-Bedia, M., 2006. Seismic Radiation from Simple Models of Earthquakes, in *Earthquakes: Radiated Energy and the Physics of Faulting*, pp. 223–236, eds Abercrombie, R., McGarr, A., Toro, G. D., & Kanamori, H., American Geophysical Union.

Mai, P. M. & Beroza, G. C., 2002. A spatial random field model to characterize complexity in earthquake slip, *Journal of Geophysical Research: Solid Earth*, **107**(B11), ESE 10–1.

Melgar, D., Fan, W., Riquelme, S., Geng, J., Liang, C., Fuentes, M., Vargas, G., Allen, R. M., Shearer, P. M., & Fielding, E. J., 2016. Slip segmentation and slow rupture to the trench during the 2015, Mw8.3 Illapel, Chile earthquake, *Geophysical Research Letters*, **43**(3), 2015GL067369.

Meng, L., Inbal, A., & Ampuero, J.-P., 2011. A window into the complexity of the dynamic rupture of the 2011 Mw 9 Tohoku-Oki earthquake, *Geophysical Research Letters*, **38**(7), L00G07.

Meng, L., Ampuero, J.-P., Luo, Y., Wu, W., & Ni, S., 2012a. Mitigating artifacts in back-projection source imaging with implications for frequency-dependent properties of the Tohoku-Oki earthquake, *Earth, Planets and Space*, **64**(12), 5.

Meng, L., Ampuero, J.-P., Stock, J., Duputel, Z., Luo, Y., & Tsai, V. C., 2012b. Earthquake in a maze: Compressional rupture branching during the 2012 Mw 8.6 Sumatra earthquake, *Science*, **337**(6095), 724–726.

Meng, L., Zhang, A., & Yagi, Y., 2016. Improving Back-Projection Imaging with a Novel Physics-Based Aftershock Calibration Approach: A Case Study of the 2015 Gorkha Earthquake, *Geophysical Research Letters*.

Meng, L., Bao, H., Huang, H., Zhang, A., Bloore, A., & Liu, Z., 2018. Double pincer movement: Encircling rupture splitting during the 2015 Mw 8.3 Illapel earthquake, *Earth and Planetary Science Letters*, **495**, 164–173.

Obara, K., Kasahara, K., Hori, S., & Okada, Y., 2005. A densely distributed high-sensitivity seismograph network in Japan:Hi-net by National Research Institute for Earth Science and DisasterPrevention, *Review of Scientific Instruments*, **76**(2), 021301.

Okada, Y., Kasahara, K., Hori, S., Obara, K., Sekiguchi, S., Fujiwara, H., & Yamamoto, A., 2004. Recent progress of seismic observation networks in Japan Hi-net, F-net, K-NET and KiK-net, *Earth, Planets and Space*, **56**(8), xv–xxviii.

Olsen, K. B. & Mayhew, J. E., 2010. Goodness-of-fit Criteria for Broadband Synthetic Seismograms, with Application to the 2008 Mw 5.4 Chino Hills, California, Earthquake, *Seismological Research Letters*, **81**(5), 715–723.

Qin, W. & Yao, H., 2017. Characteristics of subevents and three-stage rupture processes of the 2015mw 7.8 Gorkha Nepal earthquake from multiple-array back projection, *Journal of Asian Earth Sciences*, **133**, 72–79.

Rice, J. R., 1993. Spatiotemporal complexity of slip on a fault, *Journal of Geophysical Research: Solid Earth*, **98**(B6), 9885–9907.

Rost, S. & Thomas, C., 2002. Array Seismology: Methods and Applications, *Reviews of Geophysics*, **40**(3), 1008.

Schmedes, J., Archuleta, R. J., & Lavalle, D., 2010. Correlation of earthquake source parameters inferred from dynamic rupture simulations, *Journal of Geophysical Research: Solid Earth*, **115**(B3), B03304.

Schmedes, J., Archuleta, R. J., & Lavalle, D., 2013. A kinematic rupture model generator incorporating spatial interdependency of earthquake source parameters, *Geophysical Journal International*, **192**(3), 1116–1131.

Scholz, C. H., 1998. Earthquakes and friction laws, *Nature*, **391**(6662), 37–42.

Sufri, O., Koper, K. D., & Lay, T., 2012. Along-dip seismic radiation segmentation during the 2007 Mw 8.0 Pisco, Peru earthquake, *Geophysical Research Letters*, **39**(8), L08311.

Uchide, T., Yao, H., & Shearer, P. M., 2013. Spatio-temporal distribution of fault slip and high-frequency radiation of the 2010 El Mayor-Cucapah, Mexico earthquake, *Journal of Geophysical Research: Solid Earth*, **118**(4), 1546–1555.

Walker, K. T. & Shearer, P. M., 2009. Illuminating the near-sonic rupture velocities of the intracontinental Kokoxili Mw 7.8 and Denali fault Mw 7.9 strike-slip earthquakes with global P wave back projection imaging, *Journal of Geophysical Research: Solid Earth*, **114**(B2).

Walker, K. T., Ishii, M., & Shearer, P. M., 2005. Rupture details of the 28 March 2005 Sumatra Mw 8.6 earthquake imaged with teleseismic P waves, *Geophysical Research Letters*, **32**(24), L24303.

Wang, D. & Mori, J., 2011. Frequency-dependent energy radiation and fault coupling for the 2010 Mw8.8 Maule, Chile, and 2011 Mw9.0 Tohoku, Japan, earthquakes, *Geophysical Research Letters*, **38**(22), L22308.

Wang, D., Mori, J., & Uchide, T., 2012. Supershear rupture on multiple faults for the Mw 8.6 Off Northern Sumatra, Indonesia earthquake of April 11, 2012, *Geophysical Research Letters*, **39**(21).

Wang, D., Takeuchi, N., Kawakatsu, H., & Mori, J., 2016. Estimating high frequency energy radiation of large earthquakes by image deconvolution back-projection, *Earth and Planetary Science Letters*, **449**, 155–163.

Warren, L. M. & Shearer, P. M., 2000. Investigating the frequency dependence of mantle Q by stacking P and PP spectra, *Journal of Geophysical Research: Solid Earth*, **105**(B11), 25391–25402.

Warren, L. M. & Shearer, P. M., 2002. Mapping lateral variations in upper mantle attenuation by stacking P and PP spectra, *Journal of Geophysical Research: Solid Earth*, **107**(B12), 2342.

Warren, L. M. & Shearer, P. M., 2005. Using the Effects of Depth Phases on P-wave Spectra to Determine Earthquake Depths, *Bulletin of the Seismological Society of America*, **95**(1), 173–184.

Wells, D. L. & Coppersmith, K. J., 1994. New empirical relationships among magnitude, rupture length, rupture width, rupture area, and surface displacement, *Bulletin of the Seismological Society of America*, **84**(4), 974–1002.

Xu, Y., Koper, K. D., Sufri, O., Zhu, L., & Hutko, A. R., 2009. Rupture imaging of the Mw 7.9 12 May 2008 Wenchuan earthquake from back projection of teleseismic P waves, *Geochemistry, Geophysics, Geosystems*, **10**(4), Q04006.

Yagi, Y. & Okuwaki, R., 2015. Integrated seismic source model of the 2015 Gorkha, Nepal, earthquake, *Geophysical Research Letters*, **42**(15), 2015GL064995.

Yagi, Y., Nakao, A., & Kasahara, A., 2012. Smooth and rapid slip near the Japan Trench during the 2011 Tohoku-oki earthquake revealed by a hybrid back-projection method, *Earth and Planetary Science Letters*, **355-356**, 94–101.

Yao, H., Gerstoft, P., Shearer, P. M., & Mecklenbruker, C., 2011. Compressive sensing of the Tohoku-Oki Mw 9.0 earthquake: Frequency-dependent rupture modes, *Geophysical Research Letters*, **38**(20), L20310.

Yao, H., Shearer, P. M., & Gerstoft, P., 2012. Subevent location and rupture imaging using iterative backprojection for the 2011 Tohoku Mw 9.0 earthquake, *Geophysical Journal International*, **190**(2), 1152–1168.

Yao, H., Shearer, P. M., & Gerstoft, P., 2013. Compressive sensing of frequency-dependent seismic radiation from subduction zone megathrust ruptures, *Proceedings of the National Academy of Sciences*, **110**(12), 4512–4517.

Yin, J. & Yao, H., 2016. Rupture and frequency-dependent seismic radiation of the 2012 Mw 8.6 Sumatra strike-slip earthquake, *Geophysical Journal International*, **205**(3), 1682–1693.

Yin, J., Yang, H., Yao, H., & Weng, H., 2016. Coseismic radiation and stress drop during the 2015 Mw 8.3 Illapel, Chile megathrust earthquake, *Geophysical Research Letters*, **43**(4), 1520–1528.

Yin, J., Yao, H., Yang, H., Qin, W., Jing, L.-Z., & Zhang, H., 2017. Frequency-dependent rupture process, stress change, and seismogenic mechanism of the 25 April 2015 Nepal Gorkha Mw 7.8 earthquake, *SCIENCE CHINA Earth Sciences*, **60**(4), 796–808.

Yin, J., Denolle, M. A., & Yao, H., 2018. Spatial and Temporal Evolution of Earthquake Dynamics: Case Study of the Mw 8.3 Illapel Earthquake, Chile, *Journal of Geophysical Research: Solid Earth*, **123**(1), 344–367.

Yue, H., Castellanos, J. C., Yu, C., Meng, L., & Zhan, Z., 2017. Localized water reverberation phases and its impact on backprojection images, *Geophysical Research Letters*, **44**(19), 9573–9580.

Zhang, H., van der Lee, S., & Ge, Z., 2016. Multi-array rupture imaging of the devastating 2015 gorkha, nepal earthquake sequence, *Geophysical Research Letters*.